Micromotions matter: an investigation of mechanical meta-materials in the plane.

Master Thesis

Bas Bets

Delft University of Technology

TU Delft

Experimental validation of micropolar elastic constants for two-dimensional chiral mechanical metamaterials.

by

Bas Bets

Supervisor:	Prof.dr.ir. J.L. Herder
Daily supervisor:	Ir. P. Roberjot
Project Duration:	May, 2024 - June,2025
Faculty:	Faculty of Mechanical Engineering,
Department:	Department of BioMechanical Engineering Department of Precision and Microsystems Engineering
Adress:	Mekelweg 2, 2628 CD Delft, The Netherlands

TU Delft

Preface

This work concludes my Master's degree in Mechanical engineering at Delft University of Technology. In this work, I take a deep dive into a novel field of engineering research, Mechanical Metamaterials, within the Mechanical Metamaterials of Compact Motion Systems (MeCoMoS) group of the Precision and Micro-systems Engineering (PME) department. In my work, I have identified an expansion of the classical elasticity theory from continuum mechanics as a promising framework for the description of mechanical metamaterials, and attempted to validate its description for a specific set of mechanical metamaterials that exist in two-dimensional space.

Notably, this thesis diverges from the specialization of my master track BioMechanical Design. Although I sincerely enjoyed learning about nature and especially the human body through the lens of a mechanical engineer, I have found that the more abstract mathematics that drive the field of engineering are still alluring to me. Discussing this desire with several professors led me to the office of my eventual supervisor, Just Herder, where he introduced me to the MeCoMoS group in a pleasant first meeting.

Initially reading about the topic, I found it extremely interesting, both from the perspective of my master track, with research being published mentioning constructs as ”meta bio-implants”, as well as from a fundamental engineering perspective with the field drawing inspiration from mathematical concepts like group theory and combinatorics, whilst feeling like a logical successor of one of my favorite topics: compliant mechanisms. As you can imagine, my choice was quickly made, I would graduate on this topic.

Now, well over a year later, the time has come to complete the thesis. But before all of this ends, I must share my extensive gratitude to my supervisors, Just Herder and Pierre Roberjot, for their weekly meetings, interesting discussions and pleasant atmosphere. I often feel a complete chaos in my mind when ideas start to come, and you have never let me leave a meeting feeling worse. Somehow we always managed to sort out the thoughts and create clarity from the chaos. I sincerely believe this combination of friendliness and the depth of our discussions is what I most enjoyed during this project. For this I am extremely grateful, it would not have been the same without you.

Additionally, I would like to thank other members of the MeCoMoS group for their expertise, invaluable insights and assisting me in keeping the broader picture in mind. Furthermore, I would like to provide a sincere thank you to the PME lab-staff, Patrick van Holst and Spiridon van Veldhoven, with their insights for my experimental setup, helping me printing the MMs and thinking along to solve the issues that arose. Additionally, I want to thank Bradley But for his assistance in wiring up the linear stage with a 6-DOF reaction force sensor and our friendly and constructive interactions regarding the experimental setup.

Last but not least, I must thank all people who have supported me throughout this journey. Starting with my family and my girlfriend, who were always there, made the hard times bearable and have never ceased to challenge me by making me explain my thesis work. Additionally, I would like to thank the many friends, some of whom feel like family, for all the good memories, for never letting me feel alone, the mutual support during the hardest parts of the Master and for letting me sleep in their homes countless of times. I could not have completed this degree without your support, and definitely would not have enjoyed it as much as I did without you.

Bas Bets
Delft, June 2025

Summary

This thesis explores the application of micropolar elasticity theory as a comprehensive framework for describing the behavior of planar chiral mechanical metamaterials. Mechanical metamaterials (MMs), also known as architected materials, are engineered structures whose unique physical properties arise from their internal geometries consisting of repeating volume elements, rather than their base materials. These properties enable applications like wave-dispersion control, soft robotic actuators or tunable and reconfigurable motion systems.

This work begins by situating metamaterials, and especially how they are described, within the broader field of continuum mechanics, highlighting the limitations of classical elasticity in systems with high stress gradients or internal structural complexity. To address these gaps, the author proposes using a decoupled version of an expanded theory of elasticity called ”micropolar elasticity” — a generalized theory that introduces rotational degrees of freedom and additional stress-strain interactions at the micro-scale.

However, it was found that the application of this theory in the field of MMs has proven difficult. A majority of the research implemented both linear and isotropic assumptions to retrieve the elastic constants of the decoupled micropolar elastic tensor. However, no consensus was reached in the literature to what extent these assumptions are valid in the case of MMs, especially in the face of chirality. To investigate the anisotropy of these MMs in the two-dimensions, a novel two-dimensional experimental method was developed to measure all independent micropolar elastic constants of a selected tetrachiral metamaterial unit cell — the ”missing rib 4” structure. This method avoids the assumptions of linearity and isotropy common in the literature and whilst being capable of isolating micropolar effects, such as independent rotational stiffness and shear-moment coupling.

Experimental results were obtained using custom-built test setups with high-precision force and displacement sensors. Despite challenges such as significant mechanical hysteresis (attributed to interface friction), the data showed high repeatability. Post-processing successfully removed these nonlinear effects, revealing core elastic behaviors. From the measurements, 36 independent micropolar constants were calculated. These were compared to analytical models and symmetry-based theoretical predictions. Notably, discrepancies between analytical and symmetry-predicted couplings were observed, highlighting the importance of direct experimental validation in micropolar elasticity.

The findings contribute a methodology for characterizing planar metamaterials free of assumptions and demonstrate that micropolar elasticity offers predictive power beyond classical approaches. Additionally, it was found that the frequently made assumption of isotropy does not hold for the selected MM geometry. As such, the authors propose more research is needed to derive anisotropic tensors and how their change depending on the symmetries in the MM. The work closes by suggesting future research paths suggests a road-map to the development inverse design frameworks for motion-system applications.

Contents

Nomenclature

Abbreviations

Abbreviation	Definition
DME	Decoupled Micropolar Elastic(ity)
MM	Mechanical metamaterial
UC	Unit cell

Symbols

Symbol	Definition	Unit
a	Side length of the minimal structure	[mm]
h	Side thickness of the minimal structure	[mm]
θ_0	Initial angle of the minimal structure	[rad]
η	Dimensionless thickness of the minimal structure	[-]
E_b	Young's modulus of the base material	[MPa]
L	Sample length	[mm]
l	Characteristic unit cell length	[mm]
d	Displacement enforced by actuator	[mm]
r	Radius of the pulley in the rotation experiment	[mm]
u	Nodal displacement in x	[mm]
v	Nodal displacement in y	[mm]
ϕ	Nodal micro-rotation about z	[rad]
$\boldsymbol{\sigma}$	Micropolar stress tensor	N.A.
σ	Micropolar stress	[MPa]
m	Couple stress (Moment stress)	[MPa·m]
$\boldsymbol{S}$	Decoupled micropolar stress tensor	[MPa]
S	Symmetric decoupled micropolar stress	[MPa]
T	Antisymmetric decoupled micropolar stress	[MPa·m]
$\boldsymbol{\varepsilon}$	Micropolar strain tensor	N.A.
ε	Micropolar strain	[-]
φ	Couple strain (Curvature)	[rad/m]
$\boldsymbol{E}$	Decoupled micropolar strain tensor	N.A.
E	Symmetric decoupled micropolar strain	[-]
A	Antisymmetric decoupled micropolar strain	[rad/m]
λ	Lamé's first parameter	[MPa]
μ	Lamé's second parameter	[MPa]
κ	Couple modulus	[MPa]
α	Cosserat twist modulus	[MPa·m^2]
β	Cosserat twist modulus	[MPa·m^2]
γ	Cosserat twist modulus	[MPa·m^2]
A	Chiral parameter	[MPa]
B	Anisotropic constant	[MPa]
ζ	Anisotropic constant	[MPa]

1

Introduction

1.1. Background

The rapidly growing field of mechanical metamaterials (MMs), also referred to as architected structures, meta-structures or architected materials, constitute a novel class of materials with physical behavior unseen in nature. These unique behaviors are frequently used as the design goal and are achieved through the tessellation of meso-scale geometries characterized by so-called unit-cells (UC's), into the macro-scale material. These built-in geometries allow a vast design freedom, ranging from controlled mass-transport or tissue regeneration performance in meta bio-materials [30] to integrated actuators and controlled stiffness in soft robotic systems [24].

One area of interest in MMs considers the field of compact motion systems. Here, the mechanical design plays a crucial role in the motion accuracy and actuator requirements. While the field of precision mechanism design has reached maturity in recent decades through rigorous design frameworks [25] and extensive analytical solutions [28], extension of such schemes towards MM design has proven difficult.

In general, the design of MMs consists of two main aspects: the unit cell design and the tesselation of unit cells through the material. This opens up a wide design space, for example, ranging from a periodic homogeneous tesselation of centrosymmetric square UCs, to an aperiodic heterogeneous structure of varying n-fold symmetric chiral UC's tessellated in random orientations.

To aid in the design process of such MMs, various strategies have been applied in order generate designs more systematically. Presently, it was found that these strategies can be roughly categorized as follows:

1. Computational intelligence: utilizes the fast-growing field of machine learning and artificial intelligence to generate and predict suitable topological designs based on learning models. Faces limitations in predicting bulk properties, optimizing architectures, and transferring results across datasets[52];
2. Topology optimization: adjusts predefined geometric parameters or systematically removes material in low-stress areas to create an optimized geometry based on desired bulk material behavior. Also used in combination with a scale-separation framework that decomposes desired bulk behavior into local elastic requirements [44, 42, 43]. Thorough parameter analysis remains impractical and computationally expensive[20, 46];
3. Combinatorial design: utilizes theories from the mathematical field of combinatorics to systematically investigate the propagation of unit cell behavior into the tessellated structure [58, 18, 54];
4. Group theory: utilizes geometric point groups as a way of categorizing UC's and finding all potential tesselations. Symmetry groups appear useful for UC design [48, 12], whereas lattice groups systematically identify the possible space-filling tesselation [40, 19].

5. Insight: applies insights or ideas from the researchers, drawing inspiration from other fields of geometry such as paper-folding, to investigate (singular) combinations of unit cell and or tesselation;

In general, there appears to be no consensus in literature as to which strategy will lead the way, and they all have their own set of advantages and drawbacks. Some studies suggest integrating various strategies such as combinatorics and topology optimization alongside aforementioned machine learning to improve both accuracy and efficiency, reducing the computational requirements[4, 49]. However, it can not be denied that the relatively simple question of how to systematically find metamaterial geometries based on desired behavior is not yet solved[11]. Thus, it appears universally agreed that it is essential to find stronger fundamental relationships between geometry and mechanics [60, 20, 46, 11].

1.2. Problem analysis

As such, we shift to the field of materials science. Its quintessential question revolves around systematically describing, predicting and designing an abundant variety of materials for specific material properties. Continuum mechanics lies at the intersection of engineering mechanics and materials science. It provides fundamental yet functional relationships, enabling insights gained from materials science to propagate into constitutive relations and functional guidelines used in engineering.

So far, capturing isotropic and linear material behavior has essentially been solved by classical (Cauchy) elasticity theory [7]. Although Cauchy elasticity has proven extremely useful in a wide variety of settings, it is limited by its simplicity to only describe *non-centrosymmetric, linear and incompressible* materials [11], which is very limiting in the perspective of MMs. To combat these limitations, finite element methods have extended the applicability of Cauchy elasticity and serve as a baseline for the analysis of more complex geometries. However, as mentioned before, such methods do not directly contribute to a stronger understanding of the governing mechanics between meso-structure and macro-behavior and remain computationally expensive.

Due to these limitations, researchers have long been expanding and generalizing the principles of Cauchy elasticity into theories such as couple-stress theory [37, 29], micropolar theory [15, 16] and Willis' theory [57, 39]. Here, couple-stress theory allows for internal moments (or couple-stresses) to exist and aid in the deformation of the continuum, effectively adding two elastic constants (β and γ) to the material description. Micropolar elasticity, otherwise known as Cosserat elasticity, does not just allow internal moments to exist, but also allows internal rotations (or couple strains) to occur, adding another two elastic constants (κ and α). The most elaborate theories are found in the so-called micromorphic theory of elasticity [17, 53], which expand the 3 spatial degrees of freedom with a micro-distortion tensor containing 9 additional degrees of freedom for each node [11].

When choosing a constitutive model, there is a trade-off between theoretical complexity and the complexity of behavior that has to be described. For MM design, it has been found that classical descriptions such as Cauchy elasticity are unable to correctly describe their continuum. Willis' elasticity, on the other hand, is frequently and successfully applied when designing for specific electrodynamic properties. However, for designing low-frequency and static mechanical metamaterials it lacks the additional degrees of freedom allowed by other theories[39]. The couple-stress theory does allow for internal moment stresses to exist, but lacks independent rotational freedom of the micropolar nodes. Micropolar elasticity on the other hand, does allow such independent couple-strains to exist alongside the couple-stresses. Lastly, micromorphic elasticity could allow for even more detailed descriptions of MMs, but it is not yet clear to what extend the added complexity contributes to the predictive accuracy of the theory.

As such, this study adopts micropolar elasticity as the theoretical framework due to its ability to include chiral and anisotropic behavior [11] with minimal added complexity. On top of the displacements u and v of points in a lattice, it also allows nodal rotations ϕ_i of those points [16, 17]. Following the notations of Eringen[16, 17], this expands the classical set of elastic constants, volumetric stiffness (Lamé's first parameter) λ and shear stiffness (Lamé's second parameter) μ, with the micropolar modulus (couple modulus) κ, and the Cosserat twist moduli α, β and γ [17]. In this paper, the preferred notation of the micropolar theory suggested by [22] is used with some alternations to prevent confusion. An overview of all symbols used is presented in the **Nomenclature**.

On the other hand, it has proven difficult to identify the values of these micropolar elastic constants, especially when trying to derive them analytically. Lakes and Yang were the first to succeed experimentally, using bending-creep and torsion tests to measure the micropolar elastic constants through related engineering constants in materials such as human bone, polymeric foams and metallic foams [32, 31]. However, they only managed to do so by assuming isotropic behavior.

More recently, researchers have once more begun identifying the micropolar constants specifically for the development and analyses of MMs. For centrosymmetric (achiral) periodic metamaterials, the elastic tensors have been derived analytically and in closed form by Bacigalupo [1]. Origami-like metamaterials have their continuum constants be derived through homogenization as Kirchoff-Love plates [55] or using a one-dimensional beam model to identify coupling constants of couple-stress theory [9]. For fully planar chiral metamaterials, [34] uses a mono-clinic micropolar model to predict all micropolar constants of selected chiral geometries and performs both experimental and numerical validation, essentially deriving the elastic constants for a planar case. In [33] this result is expanded to three dimensional metamaterials by applying the two-dimensional case to all faces of a three-dimensional unit cell.

One study [12] finds that the internal rotations of the micropolar theory tensor can be ”decoupled” and presents what they call the Decoupled Micropolar Elasticity (DME) tensor. Based on symmetry operations they predict both presence and absence of couplings for each point group. They expand their work to three-dimensional cases in [13]. Unfortunately, in neither study do they verify their results experimentally. In a similar fashion, [48] created a minimal chiral structure and utilizes the same symmetry operations to differentiate several families of MMs based on chirality and their inherent unit cell point group.

Here, we see a potential gap. In this study we aim to validate the decoupled micropolar elastic (DME) constants as proposed by [12] for the MM families proposed by [48]. In this way, we aim to validate what couplings exist inside the MMs. However, no literature was found describing a method to validate the micropolar elastic constants of the plane. By performing physical experiments, the authors aim to find a ground-truth of potential couplings that are not affected by underlying assumptions of analytical models and finite element simulations.

1.3. Research objective

This study aims to experimentally validate of the decoupled micropolar elastic constants as described by Cui [12], using the metamaterial families proposed by Roberjot [48]. To this end, a novel experimental setup is used with the goal of finding the internal stress-tensor and using them to calculate the elastic constants, free of assumptions on the tensor entries. These results will then be compared to an analytical model of Bahaloo [2] and the predicted couplings from Cui [12]. Finally, all is put in the perspective of the design of MMs for compact motion systems, presenting a promising way forward.

1.4. Structure

The remainder of this study is organized as follows. Section 2.1 provides a comprehensive overview of micropolar elasticity, including its simplification for planar cases and the application of the decoupling method proposed by Cui [12] to a selected mechanical metamaterial unit cell. Section 2.2 details the metamaterial families classified by Roberjot [48], from which a chiral unit cell is selected based on available analytical models. Section 2.3 introduces the experimental methodology used to determine the micropolar elastic constants by solving the system of equations of the DME tensor. Section 2.4 details the physical embodiment of the experimental setup. Next, Section 3 presents the experimental results, including the retrieval of planar micropolar constants, their evolution under strain, and a comparison with analytical and theoretical models. Then, Section 4 discusses the findings in the context of existing literature, explores their implications for mechanical metamaterial design in compact motion systems, and outlines potential directions for future research. Finally, a conclusion is drawn on the validity of the results and frequent assumptions made in the literature.

2

Methods

In this chapter, an in-depth overview of micropolar elasticity is presented, followed by a planar simplification of the theory. Next, a mathematical decoupling transformation is presented and applied onto a chosen chiral unit cell.

2.1. Micropolar elasticity - an overview

One of the most fundamental fields of engineering is Continuum Mechanics. Its principles, especially the theory of linear elasticity, helped engineers to understand the behavior of materials on a functional level, opening the doors to all engineering achievements humanity has produced. From buildings close to a kilometer tall, to permanent scientific residences in Low Earth Orbit.

However, classical continuum mechanics has its limitations. This is especially true in cases where materials contain larger stress gradients (e.g. porous materials) or where materials contain load-bearing internal structures. Then, the classical theory of elasticity cannot accurately describe the material behavior properly.

2.1.1. A generalized theory of elasticity

For this reason, researchers sought to expand the theory of elasticity. Voigt was one of the first to achieve this, expanding the theory to include antisymmetric stresses, creating the first couple-stress theory of elasticity [56]. His work was further developed by the Cosserat brothers, who allowed a body to have an independent micro-rotation field alongside the displacement field [15]. Finally, Eringen included micro-inertia into the theory and coined it the micropolar theory of elasticity [16]. This micropolar theory of elasticity now contains 6 elastic constants to describe linear, homogeneous and centrally symmetric materials. These are the classical bulk modulus (Lamé's first parameter) λ and shear modulus (Lamé's second parameter) μ, the micropolar couple modulus κ, and the Cosserat twist moduli α, β and γ [17].

From the complete micropolar elastic description, it is possible to reduce to a couple-stress theory version by enforcing the couple modulus κ and first twist moduli α to infinity [23]. Thus, the internal micro-rotations are set to have infinite stiffness with respect to the macro-rotations and displacements, removing the independent micro-rotation field from the description. This couple-stress theory is thus fully defined by the four remaining elastic constants λ, μ, β and γ. Further simplification of couple-stress theory can be achieved by forcing the remaining twist-moduli, β and γ to be zero [23], leaving only the classical Lamé parameters to define the material behavior, just as in the classical theory of elasticity.

More broadly speaking, the micropolar theory of elasticity shows promise as a more useful as descriptor of materials containing additional micro- and meso structure like bone or porous materials, but their experimental validation still proves difficult aswell [23, 22]. Experiments have been performed on materials like bone and polymer foam through bending-creep and tensile-torsion tests in various studies performed by Lakes [32, 31], where they measured the engineering constants: E_m, G_m, ν_m, l_b, l_t, N and Ψ, which are expressed as functions of the elastic constants. Here, E_m, G_m and ν_m are the micropolar bulk modulus, the micropolar shear modulus and the micropolar Poisson's Ratio respectively.

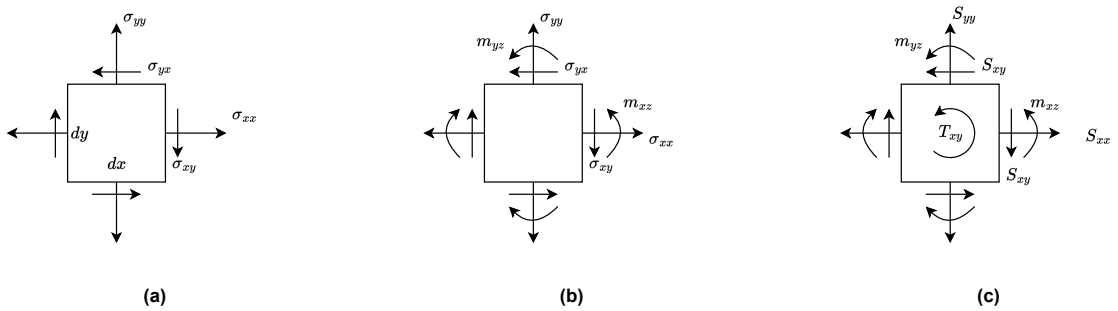

(a) **(b)** **(c)**

Figure 2.1: (a) Classical stresses on in Cauchy elasticity, showing principal σ_{xx}, σ_{yy} and shear σ_{xy}, σ_{yx} stresses. [7]. (b) Micropolar stresses in Eringen elasticity [16], showing the additional couple stresses m_{xz}, m_{yz} (representation adapted from [5]). (c) Decoupled micropolar stresses in DME, showing one symmetric shear stress S_{xy} and one (antisymmetric) internal torque stress T_{xy}, alongside the unaltered principal stresses S_{xx}, S_{yy} and couple stresses m_{xz}, m_{yz}.

Then, l_b is the characteristic length in bending, l_t is the characteristic length in Torsion, N is the coupling number and Ψ is the polar ratio. When simplified to two dimensions only the micropolar bulk modulus E_m, micropolar Poisson's ratio ν_m, characteristic length l and coupling number N survive [38], corresponding to the elastic constants of λ, μ, κ and γ. The simplification to classical elasticity is then found by setting the characteristic length l to zero [38]. The relations between the elastic and engineering constants for the planar case are:

$$l^2 = \frac{\gamma}{4\mu + 2\kappa} \tag{2.1a}$$

$$N = \frac{\kappa}{2\mu + 2\kappa} \tag{2.1b}$$

$$\nu_m = \frac{\lambda}{2\mu + 2\lambda + \kappa} \tag{2.1c}$$

$$N = \frac{(2\mu + \kappa)(3\lambda + 2\mu + \kappa)}{2\lambda + 2\mu + \kappa} \tag{2.1d}$$

2.1.2. Planar micropolar elasticity

In general micropolar elasticity, a planar continuum can be described with the following constitutive equation in index notation and following the conventions set by Eringen [17] with some exceptions to prevent confusion:

$$\begin{aligned} \sigma_{ij} &= C_{ijkl}\varepsilon_{kl} + B_{ijkl}\varphi_{kl} \\ m_{ij} &= B_{ijkl}\varepsilon_{kl} + D_{ijkl}\varphi_{kl} \end{aligned} \tag{2.2}$$

Here, $\varepsilon_{ij} = \delta u_j / \delta x_i$ represents the regular Cauchy strain tensor, whereas $\varphi_{ij} = \delta \phi_j / \delta x_i$ represents the couple strain tensor. Similarly, σ_{ij} is the Cauchy stress tensor and m_{ij} is the couple stress tensor. The indexes i, j and k, l represent the set of directions xx, xy, yx, yy, xz and yz. See [22] for a complete overview and comparison between notation styles of the symbols used in micropolar elasticity.

The classical (σ_{ij}) and couple (m_{ij}) stresses can be combined into a generalized vector form $\bar{\sigma} = \{\sigma_{xx}, \sigma_{yy}, \sigma_{xy}, \sigma_{yx}, m_{xz}, m_{yz}\}^T$. And similarly the classical (ε_{ij}) and couple (φ_{kl}) strain can be combined into $\bar{\varepsilon} = \{\varepsilon_{xx}, \varepsilon_{yy}, \varepsilon_{xy}, \varepsilon_{yx}, \varphi_{xz}, \varphi_{yz}\}^T$. Thus resulting in the standard micropolar constitutive equation $\boldsymbol{\sigma} = Q \cdot \boldsymbol{\varepsilon}$, with Q the micropolar elasticity tensor, filled with arbitrary entries C_{ij}, B_{ij} and D_{ij}.

$$\begin{Bmatrix} \sigma_{xx} \\ \sigma_{yy} \\ \sigma_{xy} \\ \sigma_{yx} \\ m_{xz} \\ m_{yz} \end{Bmatrix} = \begin{bmatrix} C_{11} & C_{12} & C_{13} & C_{14} & B_{11} & B_{12} \\ & C_{22} & C_{23} & C_{24} & B_{21} & B_{22} \\ & & C_{33} & C_{34} & B_{31} & B_{32} \\ & & & C_{44} & B_{41} & B_{42} \\ & sym & & & D_{11} & D_{12} \\ & & & & & D_{22} \end{bmatrix} \begin{Bmatrix} \varepsilon_{xx} \\ \varepsilon_{yy} \\ \varepsilon_{xy} \\ \varepsilon_{yx} \\ \varphi_{xz} \\ \varphi_{yz} \end{Bmatrix} \tag{2.3}$$

Furthermore, the micropolar strain components of ε can be derived from the local displacement field variables u, v and ϕ according to Nakamura and Lakes [38]:

$$\begin{Bmatrix} \varepsilon_{xx} \\ \varepsilon_{yy} \\ \varepsilon_{xy} \\ \varepsilon_{yx} \\ \varphi_{xz} \\ \varphi_{yz} \end{Bmatrix} = \begin{bmatrix} \frac{\partial}{\partial x} & 0 & 0 \\ 0 & \frac{\partial}{\partial y} & 0 \\ 0 & \frac{\partial}{\partial x} & -1 \\ \frac{\partial}{\partial y} & 0 & 1 \\ 0 & 0 & \frac{\partial}{\partial x} \\ 0 & 0 & \frac{\partial}{\partial y} \end{bmatrix} \begin{Bmatrix} u \\ v \\ \phi \end{Bmatrix} \tag{2.4}$$

In this study, we attempt to describe the behavior of a full metamaterial unit cell with the micropolar tensor. For this reason, the concepts of stress and strain in this micropolar description lose their original physical meaning, and can be referred to as ”meta-stress” and ”meta-strain” instead. This better indicates their separation from classical engineering quantities, as these meta-stresses and meta-strains encapsulate the volume enclosed by a unit-cell, which for a significant part consists of empty space. Nevertheless, the remainder of this study will refer to these quantities by their traditional names.

2.1.3. Decoupled micropolar elasticity

However useful the micropolar theory of elasticity is, in the above forms, it is still only valid for linear, isotropic and centrally symmetric (achiral) materials [22]. To include chiral behavior into the theory, a decoupling procedure can be applied, extracting the anti-symmetric micro-rotation from the symmetric shear strains [47, 12].

Following the decomposition of [12], the symmetric and anti-symmetric components of σ_{ij} and ε_{ij} can be separated, splitting the symmetric shear stress $S_{ij} = S_{ji}$ and strain $E_{ij} = E_{ji}$ from their anti-symmetric components $T_{ij} = -T_{ji}$ and $A_{ij} = -A_{ji}$.

$$S_{ij} = \frac{\sigma_{ij} + \sigma_{ji}}{2} = S_{ji}, \quad T_{ij} = \frac{\sigma_{ij} - \sigma_{ji}}{2} = -T_{ji} \tag{2.5}$$

$$E_{ij} = \frac{\varepsilon_{ij} + \varepsilon_{ji}}{2} = E_{ji}, \quad A_{ij} = \frac{\varepsilon_{ij} - \varepsilon_{ji}}{2} = -A_{ji} \tag{2.6}$$

Most notably, it is stated that this anti-symmetric component T_{xy} represents a stress torque and A_{xy} a strain rotation. In other words, a torque per unit area and associated dimensionless strain rotation per unit area, directly applied at a micropolar node. Furthermore, from [12] it turns out that

$$\begin{aligned} E_{xy} &= \gamma_{xy}/2 \\ A_{xy} &= \Omega - \phi, \end{aligned} \tag{2.7}$$

meaning that E_{xy} is equal to half of the pure engineering strain γ_{xy} and that A_{xy} represents a local rotation at one point as the difference between the macro rotation of the body Ω and the nodal rotation ϕ in macro coordinates at the point of interest. See [12] for a clear visual representation.

As such, the decoupled micropolar constitutive relation becomes $\boldsymbol{S} = q \cdot \boldsymbol{E}$ [12]:

$$\begin{Bmatrix} S_{xx} \\ S_{yy} \\ S_{xy} \\ T_{xy} \\ m_{xz} \\ m_{yz} \end{Bmatrix} = \begin{bmatrix} c_{11} & c_{12} & c_{13} & c_{14} & c_{15} & c_{16} \\ & c_{22} & c_{23} & c_{24} & c_{25} & c_{26} \\ & & c_{33} & c_{34} & c_{35} & c_{36} \\ & & & c_{44} & c_{45} & c_{46} \\ & sym & & & c_{55} & c_{56} \\ & & & & & c_{66} \end{bmatrix}^{q} \begin{Bmatrix} E_{xx} \\ E_{yy} \\ 2E_{xy} \\ 2A_{xy} \\ \varphi_{xz} \\ \varphi_{yz} \end{Bmatrix} \tag{2.8}$$

And relates to the original micropolar elasticity matrix Q as [12]

$$\begin{bmatrix} c_{11} & c_{12} & c_{13} & c_{14} & c_{15} & c_{16} \\ & c_{22} & c_{23} & c_{24} & c_{25} & c_{26} \\ & & c_{33} & c_{34} & c_{35} & c_{36} \\ & & & c_{44} & c_{45} & c_{46} \\ & sym & & & c_{55} & c_{56} \\ & & & & & c_{66} \end{bmatrix} = \begin{bmatrix} C_{11} & C_{12} & \frac{C_{13}+C_{14}}{2} & \frac{C_{13}-C_{14}}{2} & B_{11} & B_{12} \\ & C_{22} & \frac{C_{23}+C_{24}}{2} & \frac{C_{23}-C_{24}}{2} & B_{21} & B_{22} \\ & & \frac{C_{33}+C_{44}+2C_{34}}{4} & \frac{C_{33}-C_{44}}{2} & \frac{B_{31}+B_{41}}{2} & \frac{B_{32}+B_{42}}{2} \\ & & & \frac{C_{33}+C_{44}-2C_{34}}{4} & \frac{B_{31}-B_{41}}{2} & \frac{B_{32}-B_{42}}{2} \\ & sym & & & D_{11} & D_{12} \\ & & & & & D_{22} \end{bmatrix} \tag{2.9}$$

From this, it is worth noting that the decoupling equations only change the shear terms in the stress- and strain tensors. Those related to the principal directions (xx and yy) and those related to the curvatures (xz and yz) remain unchanged compared the standard micropolar elasticity.

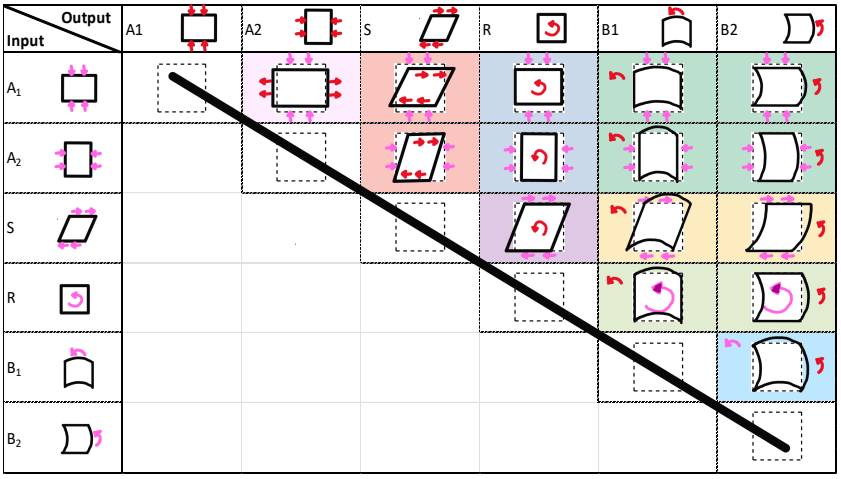

Figure 2.2: A visual representation of the couplings described by DME. Blue arrows represent an input or applied stress, the red arrows represent an output or observed strain.

Figure 2.2 shows a visual representation of the physical interpretation of each elastic constant in the DME tensor.

2.1.4. Fourfold symmetric micropolar elasticity

For a fourfold rotationally symmetric unit cell, it is then predicted to contain the following terms [12]:

$$\begin{Bmatrix} S_{xx} \\ S_{yy} \\ S_{xy} \\ T_{xy} \\ m_{xz} \\ m_{yz} \end{Bmatrix} = \begin{bmatrix} c_{11} & c_{12} & c_{13} & c_{14} & 0 & 0 \\ & c_{11} & -c_{14} & -c_{13} & 0 & 0 \\ & & c_{33} & c_{34} & 0 & 0 \\ & & & c_{33} & 0 & 0 \\ & sym & & & c_{55} & 0 \\ & & & & & c_{55} \end{bmatrix}^{q^{sym}} \begin{Bmatrix} E_{xx} \\ E_{yy} \\ 2E_{xy} \\ 2A_{xy} \\ \varphi_{xz} \\ \varphi_{yz} \end{Bmatrix}. \tag{2.10}$$

Looking at the physical implication, it is thus predicted that the fourfold symmetric unit cells can show axial-axial (E_{xx} to E_{yy}), axial-shear (E_{xx} or E_{yy} to $2E_{xy}$), axial-rotation (E_{xx} or E_{yy} to $2A_{xy}$) and shear-rotation ($2E_{xy}$ to $2A_{xy}$) couplings. A visual of all potential couplings from DME theory is shown in **Figure 2.2**. In this study, we will compare this symmetry-based prediction of the presence of decoupled elastic constants with both an analytical model of a fourfold-symmetric unit cell, and with experimentally measured elastic constants of the same unit cell.

2.2. Planar chiral mechanical metamaterials

In this study, only two-dimensional and chiral MMs are investigated. Following the work of Roberjot [48], this study examines three chiral families, consisting of the HoneyComb (Hc), Missing Rib (Mr) and Closed Geometry (Cg).

2.2.1. Chiral metamaterial families.

These three families are constructed through alternating copy-rotations of a so-called minimal auxetic structure [48]. **Figure 2.3** shows the definitions of the minimal auxetic structure, with the lengths and thicknesses of members 1 to 3 a_1, a_2, a_3 and h_1, h_2, h_3, structural depth b and the initial angle θ_0.

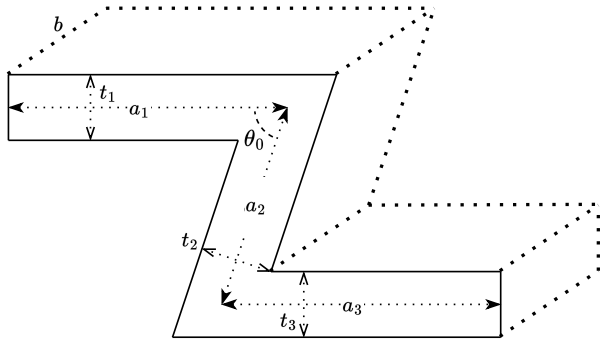

Figure 2.3: A schematic drawing of the parameters that define the minimal chiral Z. Moving from top-left to bottom right are the lengths of each element a_1 to a_3 and the thickness t_1 to t_3, as well as a universal depth b and an initial angle θ_0 between a_1 and a_2 and between a_2 and a_3.

From this minimal structure, the three chiral families: Hc, Mr and Cg, are generated according to [48], such that in

- Missing Rib: element a_3 vanishes altogether and the unit cell is bound by the endpoint of element a_1.
- Honey Comb: element a_3 vanishes into a rigid body with sides a_2 and the unit cell is bound by the endpoint of element a_1.
- Closed Geometry: element a_3 remains and the unit cell is bound by the midpoint of element a_1.

Lastly, for the remainder of this study it is assumed that all unit cells are created of minimal auxetic structures where $a_1 = a_2 = a_3 = a$ and $\theta_0 = 60$ deg, corresponding as it was found to contain the most isotropic behavior [34]. A schematic overview of the three resulting chiral families is shown in **Figure 2.4**.

2.2.2. Analytical modeling

Various studies have been deriving analytical models for chiral MMs and the most elaborate analytical relations have been derived for the Mr4 tessellated geometry [35, 10, 2, 34]. For this reason, this study will conduct experiments on the same geometry, using the existing literature for validation.

The models for the micropolar elastic tensor have been found through derivations of the strain energy density function. For geometries of $\mathbb{Z}_3$ (three-fold rotationally symmetric) and $\mathbb{Z}_6$ invariance (six-fold rotationally symmetric), these were achieved by assuming a hemitropic (isotropic except in mirroring) continuum [35]. On the other hand, [10] performs the derivation assuming an orthotropic continuum of $\mathbb{Z}_2$ (two-fold rotationally symmetric) and $\mathbb{Z}_4$ invariance (four-fold rotationally symmetric).

More recently, these isotropic and orthotropic solutions were combined to analytically derive expressions for all micropolar elastic constants specifically for the missing-rib tetra-chiral (Mr4) geometry shown on the left of **Figure 2.4** [27, 2].

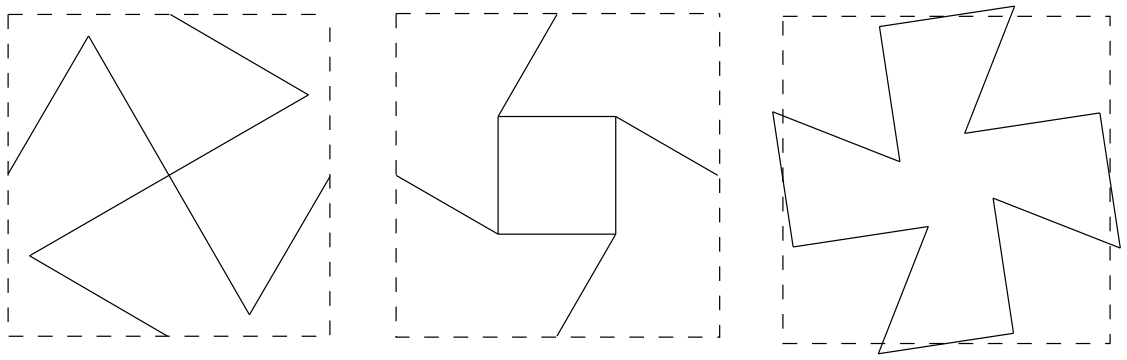

Figure 2.4: The fourfold rotationally symmetric variants of the chiral families from left to right are Missing Rib (Mr4), Honeycomb (Hc4) and Closed Geometry (Cg) shown with lengths $a_1 = a_2 = a_3$. The dashed lines shows the repeating unit of the square unit cells.

Following these derivations, the micropolar elastic tensor was separated into sub-matrices $\mathcal{C}$, $\mathcal{D}$ and $\mathcal{B}$ [35, 10, 2]. Here, $\mathcal{C}$ is a fourth order tensor describing the constitutive relations to the "regular" strains, $\mathcal{D}$ is a second order tensor describing the elasticity of the couple strains, and $\mathcal{B}$ is a third order tensor describing the coupling between the strains and couple strains.

$$\boldsymbol{\sigma} = \begin{bmatrix} \mathcal{C} & \mathcal{B} \\ \mathcal{B}^T & \mathcal{D} \end{bmatrix} \boldsymbol{\varepsilon} \tag{2.11}$$

This coupling matrix $\mathcal{B}$ is also said to contain the chiral effect, however, for two-dimensional chiral isotropic materials, it was found that $\mathcal{B} = \overline{0}$ [35]. To compensate and retain the chiral effect and include material anisotropy, $\mathcal{C}$ was decomposed into a hemitropic $\mathcal{C}^{hemi}$ [35] and a fourfold-invariant $\mathcal{C}^{4fold}$ '[10] component. Thus, the micropolar elastic tensors are defined as

$$\mathcal{C} = \mathcal{C}^{hemi} + \mathcal{C}^{4fold} = \begin{pmatrix} \lambda+2\mu & \lambda & A & -A \\ & \lambda+2\mu & A & -A \\ & & \mu+\kappa & \mu-\kappa \\ sym. & & & \mu+\kappa \end{pmatrix} + \begin{pmatrix} \zeta & -\zeta & B & B \\ & \zeta & -B & -B \\ & & -\zeta & -\zeta \\ sym. & & & -\zeta \end{pmatrix} \tag{2.12a}$$

$$\mathcal{B} = \begin{pmatrix} 0 & 0 \\ 0 & 0 \\ 0 & 0 \\ 0 & 0 \end{pmatrix} \tag{2.12b}$$

$$\mathcal{D} = \begin{pmatrix} \gamma & 0 \\ 0 & \gamma \end{pmatrix} \tag{2.12c}$$

Here, λ, μ, κ and γ are the micropolar elastic constants as described before, the parameter A is introduced to characterize the chiral effect [35], and its sign determines the handedness of chirality. The constants B and ζ are introduced to account for the anisotropy of a fourfold symmetric lattice [10]. All of these elastic constants can be analytically expressed in terms of the dimensionless thickness $\eta = h/a$, base material Young's modulus E_b and initial corner angle θ_0, which are presented in **Equations 2.14**.

Now, the individual and decomposed elastic tensors $\mathcal{C}$, $\mathcal{D}$ and $\mathcal{B}$ are assembled into the standard micropolar form of **Equation 2.3** to be

$$\begin{Bmatrix}\sigma_{xx}\\ \sigma_{yy}\\ \sigma_{xy}\\ \sigma_{yx}\\ m_{xz}\\ m_{yz}\end{Bmatrix} = \begin{bmatrix} \overbrace{\begin{bmatrix}\lambda+2\mu+\zeta & \lambda-\zeta & A+B & -A+B\\ & \lambda+2\mu+\zeta & A-B & -A-B\\ sym & & \mu+\kappa-\zeta & \mu-\kappa-\zeta\\ & & & \mu+\kappa-\zeta\end{bmatrix}}^{(\boldsymbol{\mathcal{C}})} & \mathbf{0} \\ \mathbf{0} & \overbrace{\begin{bmatrix}\gamma & 0\\ 0 & \gamma\end{bmatrix}}^{(\boldsymbol{\mathcal{D}})} \end{bmatrix} \begin{Bmatrix}\varepsilon_{xx}\\ \varepsilon_{yy}\\ \varepsilon_{xy}\\ \varepsilon_{yx}\\ \varphi_{xz}\\ \varphi_{yz}\end{Bmatrix}. \tag{2.13}$$

From [2], it was found that all elastic constants λ, μ, κ, A, B, ζ and γ of the simplified Mr4 geometry can be expressed as:

$$\mu = \frac{\eta^3 E_b \sin^2(\theta)}{8(\cos^2(\theta)+4\eta^2\sin^2(2\theta)} \tag{2.14a}$$

$$\lambda = \mu \tag{2.14b}$$

$$A = 0 \tag{2.14c}$$

$$B = \frac{\eta^3 E_b 1.5\sin(2\theta)\sin^2(\theta)}{\eta^4\sin^2(2\theta)+\eta^2[20+20\cos^2(2\theta)-24\cos(2\theta)]+28\sin^2(2\theta)} \tag{2.14d}$$

$$\gamma = \frac{E_b\eta^3\sin^2(\theta)\left\{(7+\frac{\eta^4}{4})\sin^2(2\theta)+5\eta^2[1+\cos^2(2\theta)]-6\eta^2\cos(2\theta)\right\}}{6\left\{4\sin^2(2\theta)+\eta^4\sin^2(2\theta)+5\eta^2[1+\cos^2(2\theta)]-6\eta^2\cos(2\theta)\right\}} \tag{2.14e}$$

$$\kappa = \frac{\eta^3 E_b\sin^2(\theta)\left\{(4+8\eta^2)\sin^2(\theta)-(20+8\eta^2-\eta^4)\sin^4(\theta)+16\right\}}{R^*} \tag{2.14f}$$

$$\zeta = \frac{\eta^3 E_b\sin^2(\theta)\left\{(25+\frac{\eta^4}{4})\sin^2(2\theta)+5\eta^2(1+\cos^2(2\theta)-6\eta^2\cos(2\theta)\right\}}{2R^*} \tag{2.14g}$$

where R^* is a purely geometric parameter [2]:

$$\begin{aligned} R^* = 4\{&112\sin^2(\theta)-224\sin^4(\theta)+112\sin^6(\theta)+16\eta^2\\ &+8\eta^4\sin^2(\theta)-48\eta^2\sin^2(\theta)-16\eta^4\sin^4(\theta)+140\eta^2\sin^4(\theta)\\ &+248\eta^4\sin^6(\theta)-108\eta^2\sin^6(\theta)+\eta^6\sin^4(\theta)-\eta^6\sin^6(\theta)\}. \end{aligned} \tag{2.14h}$$

Last, by applying **Equations 2.14b** and **2.14c**, the analytical relation of **Equation 2.13** simplifies to:

$$\begin{Bmatrix}\sigma_{xx}\\ \sigma_{yy}\\ \sigma_{xy}\\ \sigma_{yx}\\ m_{xz}\\ m_{yz}\end{Bmatrix} = \begin{bmatrix}3\mu+\zeta & \mu-\zeta & B & B & 0 & 0\\ & 3\mu+\zeta & -B & -B & 0 & 0\\ & & \mu+\kappa-\zeta & \mu-\kappa-\zeta & 0 & 0\\ & & & \mu+\kappa-\zeta & 0 & 0\\ & sym & & & \gamma & 0\\ & & & & & \gamma\end{bmatrix} \begin{Bmatrix}\varepsilon_{xx}\\ \varepsilon_{yy}\\ \varepsilon_{xy}\\ \varepsilon_{yx}\\ \varphi_{xz}\\ \varphi_{yz}\end{Bmatrix}. \tag{2.15}$$

2.2.3. Analytical decoupled micropolar elastic tensor

We can express it in the decoupled micropolar form. To do this, we apply the relationship of **Equation 2.9** on the simplified analytical tensor of **Equation 2.15**, resulting in:

$$\begin{Bmatrix}S_{xx}\\ S_{yy}\\ S_{xy}\\ T_{xy}\\ m_{xz}\\ m_{yz}\end{Bmatrix} = \begin{bmatrix}3\mu+\zeta & \mu-\zeta & B & 0 & 0 & 0\\ & 3\mu+\zeta & -B & 0 & 0 & 0\\ & & \kappa & 0 & 0 & 0\\ & & & 4\mu-4\zeta & 0 & 0\\ & sym & & & \gamma & 0\\ & & & & & \gamma\end{bmatrix}^{=q^{ana}} \begin{Bmatrix}E_{xx}\\ E_{yy}\\ 2E_{xy}\\ 2A_{xy}\\ \varphi_{xz}\\ \varphi_{yz}\end{Bmatrix}. \tag{2.16}$$

This analytical version of the decoupled micropolar tensor will be used in the next sections to compare against the predicted couplings by symmetry and the experimentally measured results.

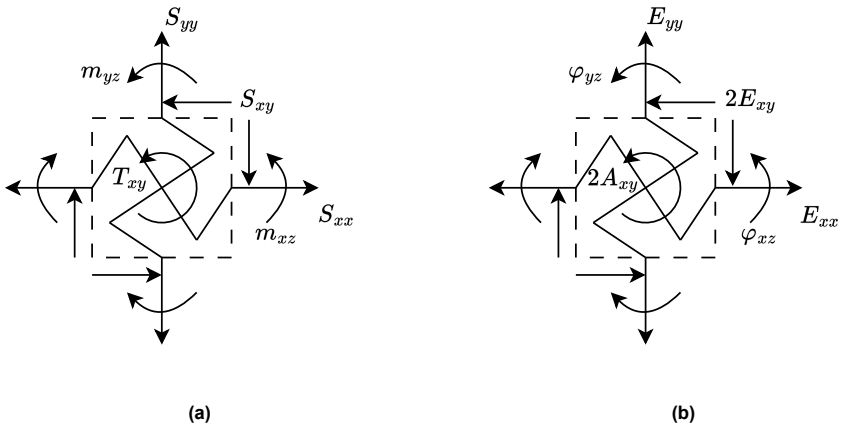

Figure 2.5: A schematic representation of all six decoupled micropolar stresses (a) and strains (b) that could exist on an Mr4 unit-cell element in the continuum.

2.3. Experimental principle

In this study, the elastic constants of DME in the plane will be investigated experimentally for the Mr4 geometry described above. To achieve this, we propose performing a separate experiment for each part of the decoupled strain vector. **Figure 2.5** shows a schematic representation of the decoupled micropolar stresses and strains acting on a unit-cell element.

By creating datasets that actuate all possible strains and attempt to measure all shown stresses. In this way, we retrieve six stress vectors $\boldsymbol{S}$ as independent functions of the six strains $\boldsymbol{E}$, this results in a total of 6 independent datasets, each containing a system of 6 equations:

1. **Uni-axial in x**, relating to E_{xx}, hereafter referred to as experiment $A1$.
2. **Uni-axial in y**, relating to E_{yy}, hereafter referred to as experiment $A2$.
3. **Symmetric shear (pure shear)**, relating to E_{xy}, hereafter referred to as experiment S.
4. **Antisymmetric shear (internal rotation)**, relating to A_{xy}, hereafter referred to as experiment R.
5. **3-point-bending over x**, relating to φ_{xz}, hereafter referred to as experiment $B1$.
6. **3-point-bending over y**, relating to φ_{yz}, hereafter referred to as experiment $B2$.

From each dataset, the authors then expand the constitutive system of equations described by the general decoupled micropolar tensor of **Equation 2.8** to find the elastic constants relating to that strain. As such there are 6 sets of 6 equations describing a maximum of 36 unknowns c_{ij}.

By the nature of the single-actuator experimental setup (with displacement d), it was practically infeasible to perform a symmetric shear experiment. Instead, two simple shear experiments, $S1$ and $S2$, are performed. By doing this, we can make use of the decoupling equations, presented in **Equation 2.5** to retrieve a ”symmetric” and an ”antisymmetric” shear experiment, named S and A respectively.

Next to the antisymmetric shear experiment, a separate internal rotation experiment is performed. This experiment is separated into a clockwise R_c and counterclockwise R_{cc} experiment due to one-directional loading capacity of wire on the spool (with diameter r). It should be noted that this now leaves a total of 7 datasets, as the antisymmetric shear experiment and the internal rotation experiment will measure the same strain component A_{xy}. The additional internal rotation experiment is performed to ensure the elastic constants relating to this strain can always be isolated and calculated, effectively reducing the likelihood that the system of equations becomes under-constrained.

All other experiments were directly performed in both positive and negative displacements. As such, a total of 8 experiments were conducted, yielding the datasets for the 6 decoupled micropolar strains in both positive and negative displacement. An overview of all experiments, applied deformations d and constraints is given in **Table 2.1**.

In **Table 2.1** u and v are the applied deformations along the x- and y-axis respectively and the forced internal rotation d/r relates to the applied micro-rotation strain ϕ. Ω represents the macro-rotation of the sample and ϕ represents the micro-rotations of each unit-cell, which are either unconstrained ($A1$, $A2$, $S1$, $S2$, $B1$, $B2$) or actuated (R_c, R_{cc}) in each experiment. An overview of these deformations for each experiment type (Axial, Shear, Bending and Rotation) is shown in **Figure 2.6**.

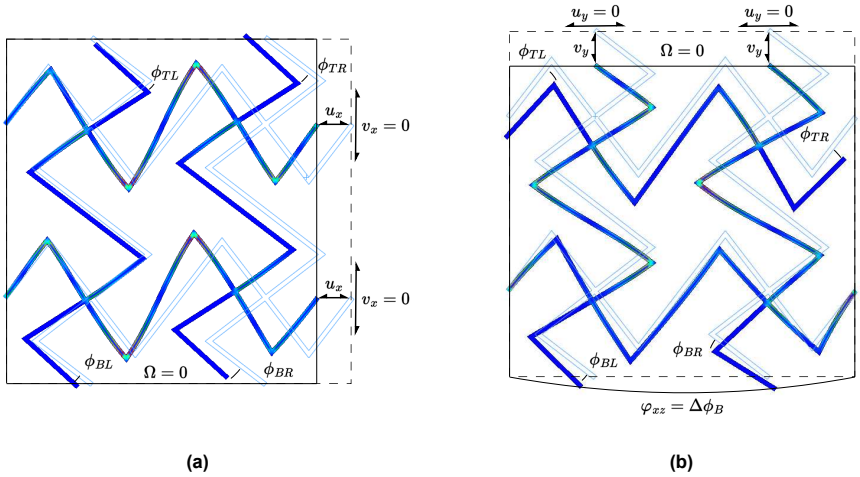

Figure 2.6: Representative displacement fields of (a): the axial experiments and (b): the bending experiments.

Table 2.1: An overview of all performed experiments, the forced displacement d, direct constraints on the boundaries, implicit rotational constraints from the boundary constraints and the free displacements that have to be measured.

$A1$	$d = u_x$	$v_x, u_y, v_y = 0$	$\Omega = 0$	ϕ
$A2$	$d = v_y$	$u_x, v_x, u_y = 0$	$\Omega = 0$	ϕ
$S1$	$d = u_y$	$u_x, v_x, v_y = 0$	-	Ω, ϕ
$S2$	$d = v_x$	$u_x, u_y, v_y = 0$	-	Ω, ϕ
$B1$	$d = v_y$	$u_x, v_x, u_y = 0$	$\Omega = 0$	ϕ
$B2$	$d = u_x$	$v_x, u_y, v_y = 0$	$\Omega = 0$	ϕ
R_c	$d/r \sim \phi$	$u_x, u_y, v_x, v_y = 0$	$\Omega = 0$	-
R_{cc}	$d/r \sim \phi$	$u_x, u_y, v_x, v_y = 0$	$\Omega = 0$	-

2.3.1. Relating displacements to decoupled meta-strains

Applying the deformation field of each experiment, as described in **Table 2.1** to the strain definitions of **Equation 2.4**, the strain tensors of each experiment can be derived.

Since the deformations u and v are forced by a displacement d in each experiment and the micro-rotations ϕ are tracked for each UC, the corresponding micropolar strain ε tensor can be calculated based on the sample length L. **Equation 2.4** can then be expanded for each experiment, resulting in the strain measurements shown in Table 2.2. Here, the partial derivatives of the displacements u and v are incorporated by dividing them by the sample length. The shear strains ε_{xy} and ε_{yx} have their internal rotation ϕ calculated as the average measured micro-rotation of all four nodes of the sample. The curvatures φ are calculated as the difference in micro-rotation between opposing free sides. Lastly, the principal strains induced for the curvature experiments are found as the difference in displacement between the actuated and the curving side.

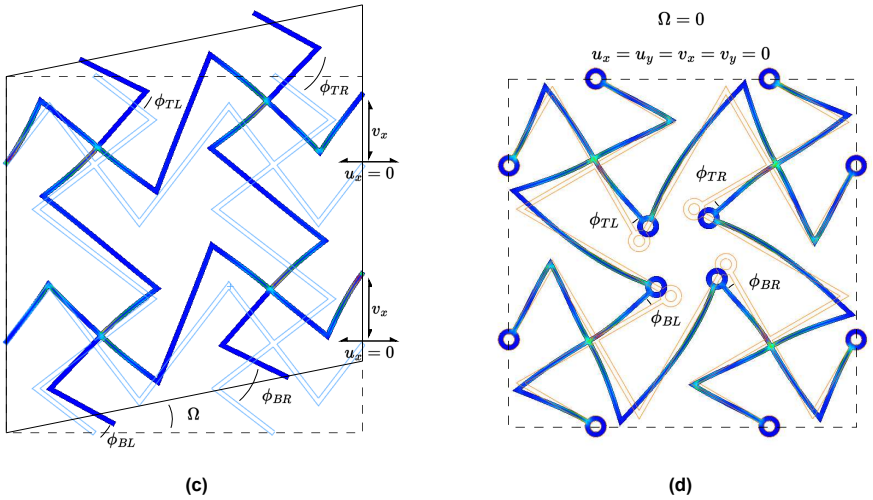

(c) (d)

Figure 2.6: Representative displacement fields of (c): the shear experiments and (d): the rotation experiment.

Table 2.2: An overview of all performed experiments with their standard micropolar strains, showing which strains are forced by the displacement d, tracked as a function of d, or assumed to be zero.

Uni-axial in x	d/L	0	$-\phi$	ϕ	$\Delta\phi_x/L$	$\Delta\phi_y/L$
Uni-axial in y	0	d/L	ϕ	$-\phi$	$\Delta\phi_x/L$	$\Delta\phi_y/L$
Simple shear on x	0	0	$d/L-\phi$	ϕ	$\Delta\phi_x/L$	$\Delta\phi_y/L$
Simple shear on y	0	0	ϕ	$d/L-\phi$	$\Delta\phi_x/L$	$\Delta\phi_y/L$
3-point bending over x	0	$\Delta v_y/L$	0	0	$\Delta\phi_x$	0
3-point bending over y	Δ_x/L	0	0	0	0	$\Delta\phi_y$
Clockwise	0	0	$-\phi$	ϕ	0	0
Counterclockwise	0	0	$-\phi$	ϕ	0	0

It should be noted that the clockwise and counterclockwise are actuated with a prescribed internal rotation d/r, but the measured micro-rotations are used in the strain tensors as they more accurately describe the deformation effect. These experiments act as a separate and completely decoupled actuation of the nodal rotations A_{xy}.

To turn the simple shear experiment into decoupled symmetric and antisymmetric shear, the decoupling formulae presented in **Equation 2.5** are applied twice. First, onto the strain tensors ε of experiment $S1$ and $S2$ as a whole. This creates a derived symmetric experiment (named S) and antisymmetric experiment (named A):

$$\varepsilon^{\boldsymbol{S}} = \frac{\varepsilon^{\boldsymbol{S1}} + \varepsilon^{\boldsymbol{S2}}}{2} \quad \& \quad \varepsilon^{\boldsymbol{A}} = \frac{\varepsilon^{\boldsymbol{S1}} - \varepsilon^{\boldsymbol{S2}}}{2} \tag{2.17}$$

Then, the decoupling equations are applied on the datasets of each experiment, extracting the decoupled strain tensors $\boldsymbol{E}$. **Table 2.3** shows this decoupled strain field as a function of the applied displacements d and and sample length L for all experiments.

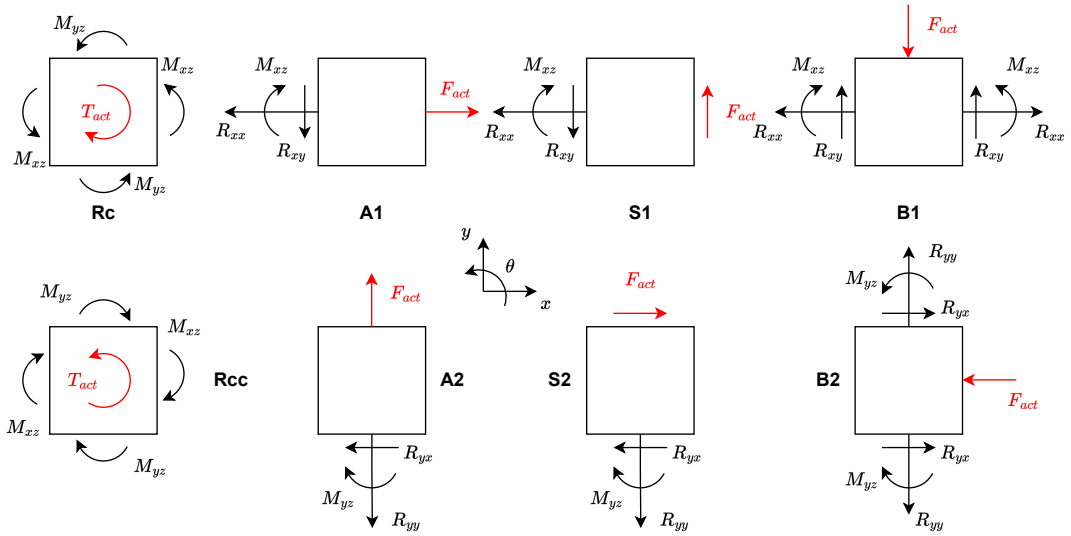

Figure 2.7: A figure showing a schematic representation of actuation and reaction forces for all experiments.

Table 2.3: An overview of all performed experiments and their decoupled micropolar strains, showing which strains are forced by the displacement d, tracked as a function of d, or constrained to be zero.

Uni-axial in x	d/L	0	0	-2ϕ	$\Delta\phi_x/L$	$\Delta\phi_y/L$
Uni-axial in y	0	d/L	0	-2ϕ	$\Delta\phi_x/L$	$\Delta\phi_y/L$
Symmetric shear	0	0	d/L	0	$\Delta\phi_x/L$	$\Delta\phi_y/L$
Antisym. shear	0	0	0	$d/L-2\phi$	$\Delta\phi_x/L$	$\Delta\phi_y/L$
3-point bending in x	0	$<d/L$	0	-2ϕ	$\Delta\phi_x/L$	0
3-point bending in y	$<d/L$	0	0	-2ϕ	0	$\Delta\phi_y/L$
Rotation	0	0	0	-2ϕ	0	0

Based on the motion tracking results, all off diagonal strains of the top six experiments might be set to zero if they are tracked to be insignificant. In this study, we assume these ”parasitic” strains to be insignificant if their signal strength is less than 10% of the dominant strain signal strength. Similarly, the curvature strains φ might be set to zero for the axial and shear experiments as well.

For the bending experiment, the axial-strains E_{xx} and E_{yy} are used to apply the moment. However, due to the inherent compressibility of the structures, this also results in a strain deformation alongside the curvature deformation. The significance of this effect and how it is dealt with will be discussed in **Section 3.1.2**.

2.3.2. Relating reaction loads to decoupled meta-stresses

Next to the strains, the stresses and couple stresses have to be determined. An overview of the free-body-diagrams relating the actuator load, reaction forces and sensor measurements is presented in **Appendix A**. A schematic representation of the reaction-forces for each experiment is shown in Figure 2.7.

From the derivations in **Appendix A**, the reaction forces contribute to the decoupled micropolar stresses as shown in **Table 2.4**.

Table 2.4: An overview of the reduced datasets and their decoupled micropolar stresses, showing which reaction forces are used to calculate them. For the stress calculation, all terms in this table are divided by the cross-sectional area of the UC.

Uni-axial in x	$-F_y$	0	$\frac{1}{2}F_x$	$\frac{1}{2}F_x - M_z - \frac{L}{2}F_x$	0	0
Uni-axial in y	0	$-F_y$	$\frac{1}{2}F_x$	$\frac{1}{2}F_x - M_z - \frac{L}{2}F_x$	0	0
Symmetric shear	$\frac{1}{2}F_x$	$\frac{1}{2}F_x$	$-\frac{1}{2}F_y$	0	0	0
Antisymm. shear	$\frac{1}{2}F_x$	$\frac{1}{2}F_x$	0	$(\frac{1}{2} - \frac{L}{2})F_y - M_z$	0	0
3-point bending in x	0	F_y	$\frac{1}{2}F_x$	$\frac{1}{2}F_x + M_z - \frac{L}{4}F_x$	LF_y	0
3-point bending in y	F_y	0	$\frac{1}{2}F_x$	$\frac{1}{2} + M_z - \frac{L}{4}F_x$	0	LF_y
Clockwise	0	0	0	M_z	0	0
Counterclockwise	0	0	0	M_z	0	0

It should be noted that all couple-stresses of the non-bending experiment are set to zero. This stems from the fact that moments inherently lack an attachment point in the plane, resulting in it being physically impossible to differentiate between a moment being applied on the x-face or on the y-face for the experiment setup used in this study. Only for the bending experiments can it be assumed on which face the moment is present, as it is induced there.

2.3.3. Solving the system of equations

Applied the forced and tracked strains onto the general DME tensor of Equation 2.8, the complete system of equations can be expanded and simplified by removing the zero-strain terms. For example, the system of equations for the symmetric shear experiment, when assuming that the curvatures φ_{xz} and φ_{yz} are measured to be zero, becomes:

$$\begin{array}{l} S_{xx} = 2c_{31}E_{xy} \\ S_{yy} = 2c_{32}E_{xy} \\ S_{xy} = 2c_{33}E_{xy} \\ T_{xy} = 2c_{34}E_{xy} \\ m_{xz} = 2c_{35}E_{xy} \\ m_{yz} = 2c_{36}E_{xy} \end{array} \quad \longrightarrow \quad \begin{array}{l} c_{31} = S_{xx}/2E_{xy} \\ c_{32} = S_{yy}/2E_{xy} \\ c_{33} = S_{xy}/2E_{xy} \\ c_{34} = T_{xy}/2E_{xy} \\ c_{35} = m_{xz}/2E_{xy} \\ c_{36} = m_{yz}/2E_{xy} \end{array} \tag{2.18}$$

Applying the stress definitions of Table 2.4, we have six equations containing six unknowns. As such, the system can be solved, finding the six elastic constants relating to E_{xy} strain. It should be noted that when the curvature φ_{yz} is not measured to be zero, the individual elastic constants can not be retrieved in this case.

2.4. Embodiment

In this section, the experimental setup, tools, experiment plates and experimented samples are presented, showcasing the used equipment, analysis tools, design parameters and fabrication processes.

2.4.1. Experimental setup

Conventional methods for measuring micropolar elastic constants are performed via the tensile-torsional deformation of the micropolar solid. However, such experiments are infeasible when investigating two dimensional structures. For this reason, this study implements conventional axial, shear and bending tests to measure the micropolar elastic constants in the plane.

2.4.2. Tools

To measure the reaction forces on the fixed end of the MM sample, an ATI 6 DOF sensor is used (±2 Nm, ±150 N, 0.25% accuracy). For measuring the free deformations based on the internal rotation, a video camera is used. All deformations were applied using a single-axis linear actuator, which ensures minimal backlash and high repeatability (1 µm resolution, 0.1 step size).

To perform the motion tracking, Kinovea software [8] is implemented to measure the local rotations of each unit cell. In this way, the strain measures of ϕ, φ_{xy} and φ_{xz} will be measured. **Figure 2.6** shows the rotations measured by Kinovea as the rotations of the free ends of each unit cell. These free ends correspond with the micro-rotation at the center of the unit cell, as these free ends are unloaded. The retrieved data is processed in MATLAB software. The complete experimental protocol is detailed in **Appendix B**.

2.4.3. Experiment plates

To perform the experiments, three plates where produced on which all 8 experiments are performed. For the purpose of fast prototyping, the linear guides enabling the displacement in the experimental plates are manufactured from 3D printed Poly-lactic Acid (PLA). A tolerance of 0.15mm between the base-plate and actuated slider was found to ensure smooth motion without excessive play.

To improve repeatability and reduce the effect of surface defects, a sanding paste was applied between the actuated sliders and the guide slots and the interface was ground down for 3 minutes. After the sanding paste was cleaned off, a layer of grease was applied. The grease increased the friction between the surfaces, but was found to increase the repeatability of the experiments. This process was repeated for all three experiment plates.

Top and side views of the three experimental plates are shown in **Figure 2.8**. The square grid of holes in each plate is used for clamping the MM samples in place. The holes are designed to align with the endpoints of a one-by-one, two-by-two or three-by-three tessellated grid of Mr4 unit cells. The square grid is of size 100 by $100\ mm$, which is the size all samples will be printed as.

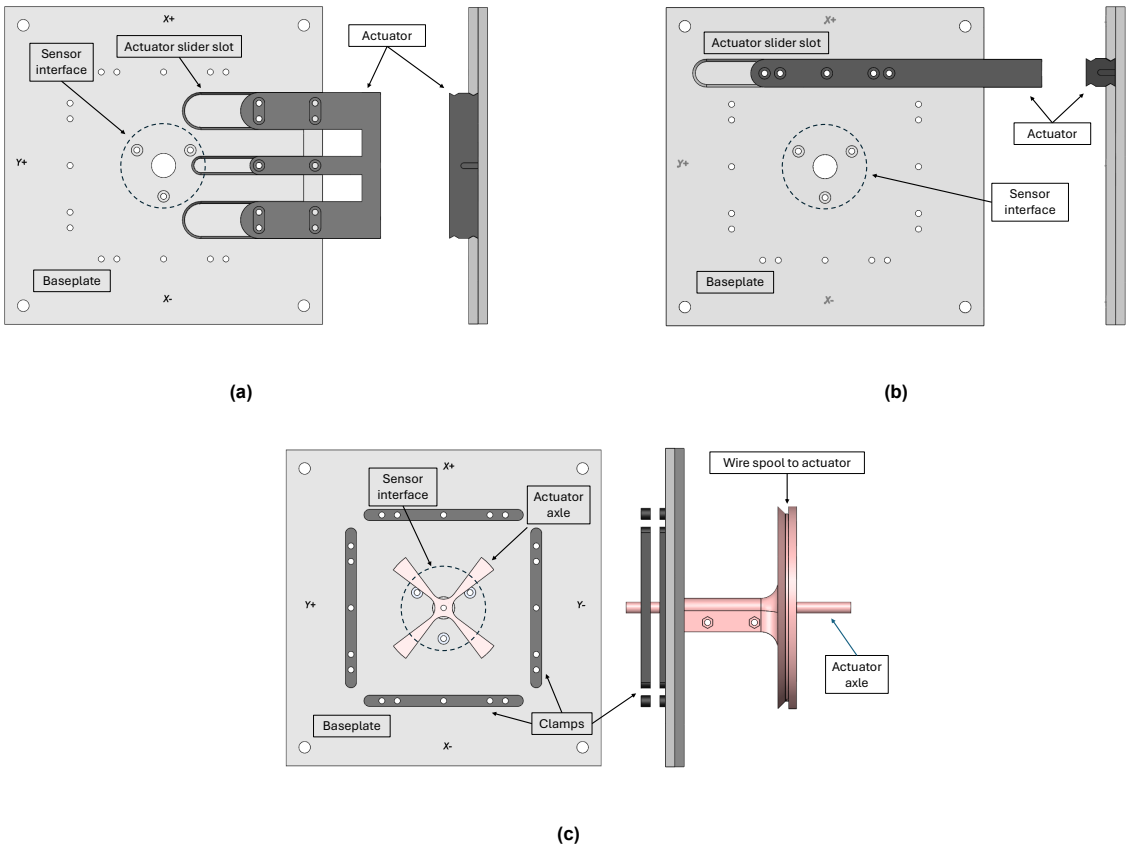

Figure 2.8: The experimental plates for all experiments. (a) the plate for axial and bending experiments, (b) the plate for shear experiments, and (c) the plate for the rotation experiments.

2.4.4. Experimented samples

The Mr4 tesselation and its parameters shown schematically in **Figure 2.9**. Here, L is the specimen size, which constitutes of n tessellations of the UC with a characteristic length l. Furthermore, the parameters h and a can be combined into a dimensionless thickness $\eta = h/a$. As such, there are a total of three parameters that fully define the Mr4 geometry: dimensionless thickness η, initial angle θ_0, and Young's Modulus of the constituent material E_b.

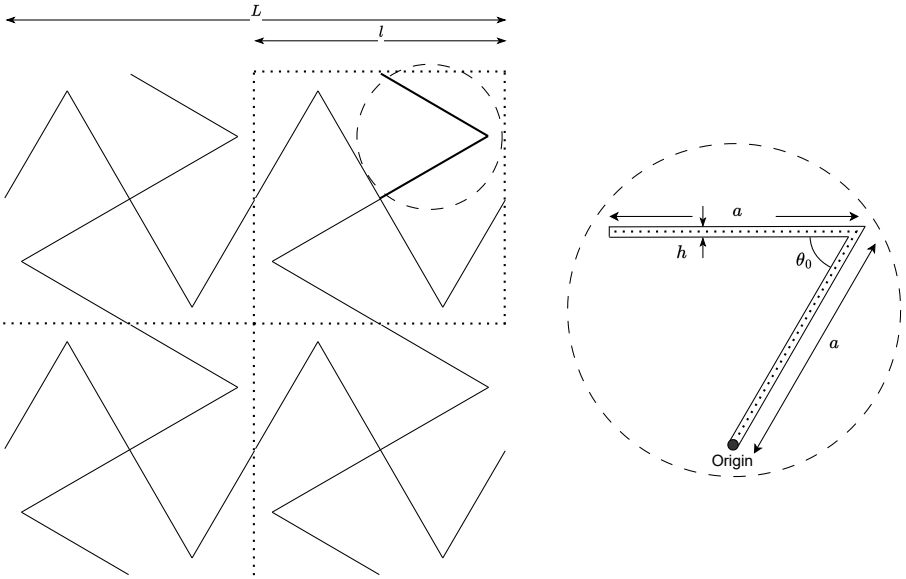

Figure 2.9: Left: the Mr4 lattice with unit cell boundaries shown. Right: the minimal Z structure with element lengths a, element thicknesses h and initial angle θ_0.

Scaling unit cells

To scale the unit cells such that they fit onto the experimental setup, the dimensionless thickness η can be used. Since the elastic tensor of Mr4 is fully defined by the three parameters η, θ_0 and E_b in **Equations 2.14**, it should follow that scale of the Mr4 UC can be altered without changing the observed behavior as long as the three parameters remain unchanged. Thus, with $\eta = h/a$, it is possible to choose the element length a to any desired length such that the total sample length L fits into the experimental setup, as long as the element thickness h is scaled inversely. For Mr4 the characteristic length l of the unit cell can be found using trigonometric identities to be:

$$l_{Mr4} = 2a\sqrt{2 - 2cos(\theta_0)} \tag{2.19}$$

(2.20)

For square lattices, it can then be said that the sample size L_4 is simply $L_4 = n * l$. With this relation, it becomes possible to find the required element lengths a, for a fixed angle θ, a fixed sample size L, and a given tessellation number n.

Table 2.5: The geometric parameters of the analyzed geometries.

Mr4	1	60	100	100	50.0	2.5	0.05
	2	60	100	50.0	25.0	1.3	0.05
	3	60	100	33.3	16.7	0.8	0.05

Based on preliminary experiments, it was found that choosing $\eta = 0.05$ showed reasonable stiffness behavior with respect to the sensor sensitivity and force limits. Based on this choice, **Table 2.5** shows an overview of all parameters for a one-by-one, two-by-two and three-by-three tessellation of the Mr4 geometry. *Due to temporal limitations, only the two-by-two sample is fully analyzed and included in this study.*

Manufacturing

For the experiments, the samples were manufactured by 3D printing technology of the Poly-ethylene Terephthalate Glycol (PETG) material. This material shows more flexible behavior compared to other frequently used materials like PLA and ABS and shows less viscoelastic behavior as compared to TPU, whilst still being safe and easy to print on FDM printers [50, 26]. This balance of material-properties makes PETG a frequently used material in compliant mechanisms and MM research [51, 6], and is why it is used in this study as well.

The metamaterial samples are printed according to **Table 2.5**, with an out-of-plane thickness of $b = 5$mm. For the print settings, the following combination of parameters provided minimal stringing between walls and minimal agglomeration of material at layer seams.

Table 2.6: Used conditions for FDM 3D printing of PETG samples.

printer	Prusa MK3S
material	PETG
nozzle diameter	0.4 mm
printing temperature	230 °C
bed temperature	25 °C
retraction length	1.5 mm
lift height	0.1 mm
infill density	25 %
infill pattern	Gyroid
layer height	0.1 mm
seam position	Random
sample orientation	Flat on built-plate

It should be noted that a relatively low infill percentage is used. This is done due to the small wall thickness of the experimented samples. This was found to improve surface finish of the printed samples. Perhaps that by leaving the infill low, this allows any over-extruded or excess material to flow to the inside instead of accumulating on the outer surface.

No further investigation was conducted on the numerical influence of printing parameters on the printed material properties. The effective Young's modulus of the base material was found by fitting the results of Finite Element simulations to the performed experiments. This is detailed further in **Section 3.2**.

3

Results

In this section, the raw experiment results of the force sensors are presented, and their processing is detailed. Next, a similar principal is applied for the strain measurements extracted through motion tracking. These results are then combined and the elastic constants are derived. Finally, the analytical tensor is computed as well, such that a fair comparison can be made.

3.1. Experimental measurements

First, the experimental measurements are presented, starting with the force sensor data. After, the motion tracking data is presented, after which these are combined to find the elastic constants. Lastly, the internal rotation experiment is detailed.

3.1.1. Sensor measurements.

In the force sensor data, significant hysteresis was found to be present.

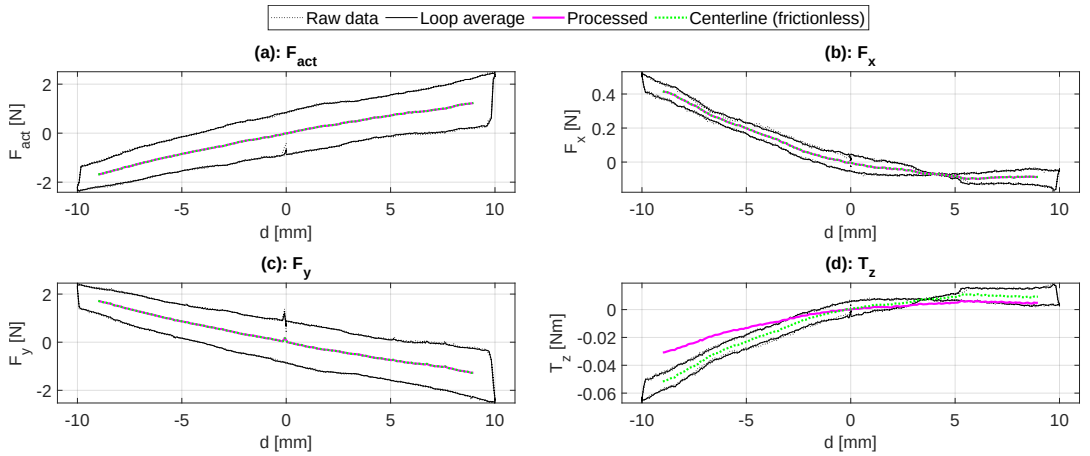

Figure 3.1: The force-displacement measurements of the actuator F_{act} (a) and the measured reaction forces F_x (b), F_y (c) and M_z (d) from the $A1$ experiment. The thin dotted lines represent the raw experimental data, solid black shows the average over loops, green dotted shows the centerline between displacement directions and the solid blue line shows the processed result removing the shear-moment coupling.

Figure 3.1 shows an example of the force-displacement measurements from the $A1$ experiment. The black dotted lines are the raw measurements containing all repetitions of the experiment. The solid black line shows the average signal over the loops. The solid yellow line shows the mid-point between the two actuation directions, essentially removing the sliding friction effect. Last, the red line shows a polynomial fitted function on the centerline. This process is shown for all measurements of all experiments in **Appendix D**.

Furthermore, the reaction force F_y opposes the displacement induced load at the actuator F_{act}, as would be expected. On the other hand, the coupling between shear loads on the base-plate and the measured reaction moment also appears perfectly inverse. This stems from the fact that the shear-coupling inside the MM sample creates reaction forces at the interface with the plate attached to the sensor. Since these reaction forces are not equal and opposite with respect to the sensor, a moment is induced. A more detailed analysis of these coupled measurements and how they are removed from the stiffness vectors is provided in **Appendix A**.

Next, the offsets at $d = 0$ and the coupled measurements are removed from the sensor dataset. Besides this, the clockwise and anti-clockwise datasets are combined. **Figure 3.1** shows an example of the removed influence of F_x on the reaction moment measurement M_z. All decoupled results and a list of removed offsets are shown in **Appendix D**.

The decoupled measurements are then used in the stress-definitions calculated in **Appendix A**. Please note that the combined shear-moment measurements as derived in this appendix have already been removed, as described above, and are not subtracted again. This results in the calculated micropolar stresses as a function of the applied displacement d shown in **Figure 3.2**.

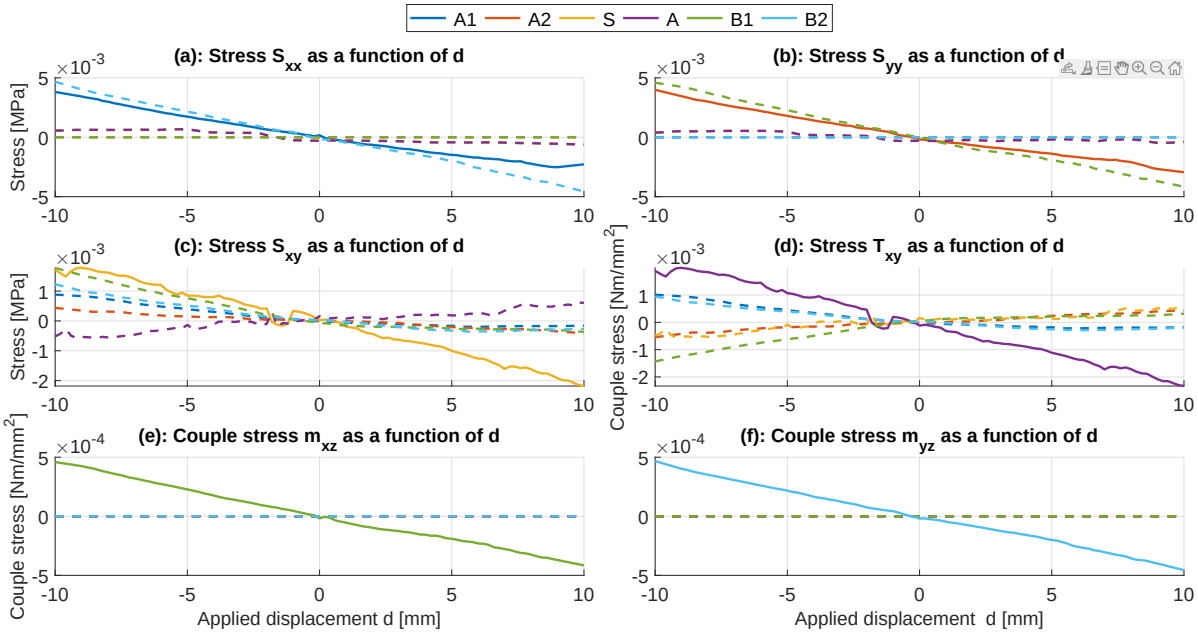

Figure 3.2: The decoupled micropolar stresses (The components of $\boldsymbol{S}$) as a function of the forced deformation d for each experiment. The solid lines represent the stress corresponding with its primary experiment, whereas the dashed lines represent that stress in the other experiments. Thus, for experiment $A1$ the stress S_{xx}, shown in (a), is the primary stress so line $A1$ is solid, for S_{yy} (b), the line corresponding to $A2$ is solid, etc.

Now that all the decoupled micropolar stresses are detailed, in the next section the decoupled micropolar strains are presented.

3.1.2. Motion tracking measurements.

In the motion tracking, the applied displacement d was measured alongside the internal rotations φ. The applied displacement is tracked to make sure the measured internal rotations can be mapped to the correct stresses from the reaction force sensor, which are also known as a function of the applied displacement. As such, the strain tensors can be set according to **Table 2.2**. Following this, the simple shear experiments are mathematically combined into a symmetric and antisymmetric experiment S and A. Now, all 7 experimental datasets are decoupled according to **Equations 2.5**.

Figure 3.3 shows the flow from measured micro-rotation and displacement toward the derived decoupled symmetric and antisymmetric shear experiments. Note that in the derived symmetric experiment, the antisymmetric strain vanishes $A_{xy} = 0$, and in the derived antisymmetric experiment that the symmetric strain vanishes $E_{xy} = 0$.

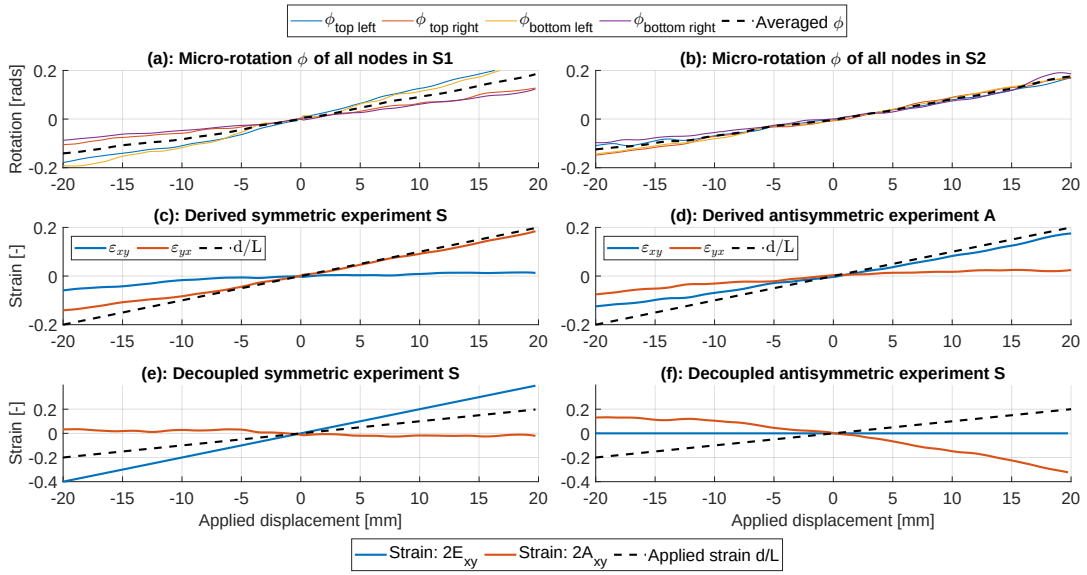

Figure 3.3: The tracked micro-rotations ϕ of the two simple shear experiments, $s1$ in (a) and $S2$ in (b). The dashed black line in (a-b) shows the averaged micro-rotation of each node in the $S1$ and $S2$ experiments. Below these, the shear strains $\varepsilon_{xy}, \varepsilon_{yx}$ of the derived symmetric (c) and antisymmetric (d) experiment, and the decoupled micropolar strains E_{xy} and A_{xy} for the derived symmetric (e) and antisymmetric (f) experiment. The dashed black line in (c-f) shows the forced simple shear strain of the $S1$ and $S2$ experiments.

Next, we investigate which unconstrained internal strains A_{xy}, φ_{xz} and φ_{yz} can be neglected. Additionally, we measure the axial strain in the bending experiments to investigate its prominence.

To asses this, we examine the relative strengths of the strains with respect to the primary actuated strain. Based on **Figure 3.4**, the internal rotation strain A_{xy} shows significant presence in the axial, antisymmetric shear and bending experiments. On the other hand, the couple strains φ_{xz} and φ_{yz} appear prominent in the bending experiments $B1$ and $B2$ only.

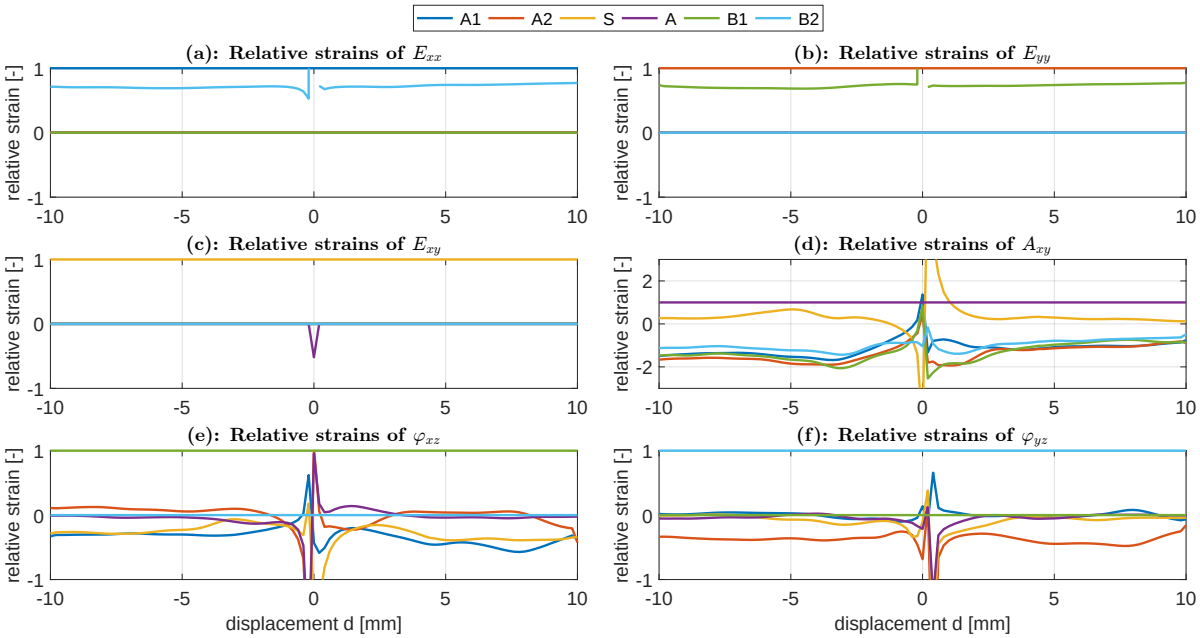

Figure 3.4: The decoupled micropolar strains, E_{xx} (a), E_{yy} (b), E_{xy} (c), A_{xy} (d), φ_{xz} (e) and φ_{yz} (f), relative to the designed dominant strains as a function of the forced displacement d for each experiment. Thus, $E_{xx} = 1$ for experiment $A1$, $E_{yy} = 1$ for experiment $A2$, etc. The singularity visible around $d = 0$ stems from the fact that it corresponds with a zero value of the primary strain, resulting in an undefined/infinite relative strain.

By taking the mean of the relative strain value at the extreme deformations ($d = -10$ and $d = 10$ mm) we ignore the singularities in the signals that occur around $d = 0$. **Table 3.1** then shows the relative strength of each of the kinematically measured strains and lists if they are assumed zero or not. By setting the threshold for assuming a strain is insignificant at 36% of the primary strain signal (diagonals on the matrix) we can simplify the system of equations, making it solvable.

Table 3.1: The relative strength of the rotation-related strains with respect to the actuated strain for each experiment. When a strain strength is smaller or equal to 0.36, it is assumed insignificant and neglected, otherwise it is included. The primary strains are the diagonal strains with respect to themselves. Since E_{xx}, E_{yy} and E_{xy} are not tracked they do not show a primary strain in the table. A_{xy}, φ_{xz} and φ_{yz} are the primary strains of experiment A, B1 and B2 respectively.

A1	A_{xy}	-1.1	Included
	φ_{xz}	0.36	Neglected
	φ_{xz}	0.02	Neglected
A2	A_{xy}	-1.3	Included
	φ_{xz}	0.10	Neglected
	φ_{xz}	0.25	Neglected
S	A_{xy}	0.19	Neglected
	φ_{xz}	0.32	Neglected
	φ_{xz}	0.22	Neglected
A	A_{xy}	1	Primary
	φ_{xz}	0.02	Neglected
	φ_{xz}	0.03	Neglected
B1	E_{yy}	0.76	Included
	A_{xy}	1.13	Included
	φ_{xz}	1	Primary
	φ_{xz}	0	Defined zero
B2	E_{xx}	0.74	Included
	A_{xy}	0.74	Included
	φ_{xz}	0	Defined zero
	φ_{xz}	1	Primary

By applying these results onto **Table 2.3**, we can retrieve an overview of the strains in the experiment as shown in **Table 3.2**.

Table 3.2: An updated overview of all performed experiments their decoupled micropolar strains, showing which strains are forced by the displacement d, which strains are tracked (ϕ) and which strains are assumed to be zero.

Uni-axial in x	d/L	0	0	-2ϕ	0	0
Uni-axial in y	0	d/L	0	-2ϕ	0	0
Symmetric shear	0	0	d/L	0	0	0
Antisym. shear	0	0	0	$d/L - 2\phi$	0	0
3-point bending in x	0	$< d/L$	0	-2ϕ	$\Delta\phi_x/L$	0
3-point bending in y	$< d/L$	0	0	-2ϕ	0	$\Delta\phi_y/L$
Rotation	0	0	0	-2ϕ	0	0

Now that both stress tensors and the strain tensors are fully set for each experiment, the system of equations can be solved. This is detailed in **Appendix E**.

3.1.3. Experimental values for the decoupled micropolar elastic tensor

By solving the system of equations as detailed in **Appendix E**, we have managed to derive all 36 possible elastic constants for the DME tensor for a planar missing-rib 4 geometry. **Figure 3.5** shows all 36 elastic constants as a function of the applied displacement d.

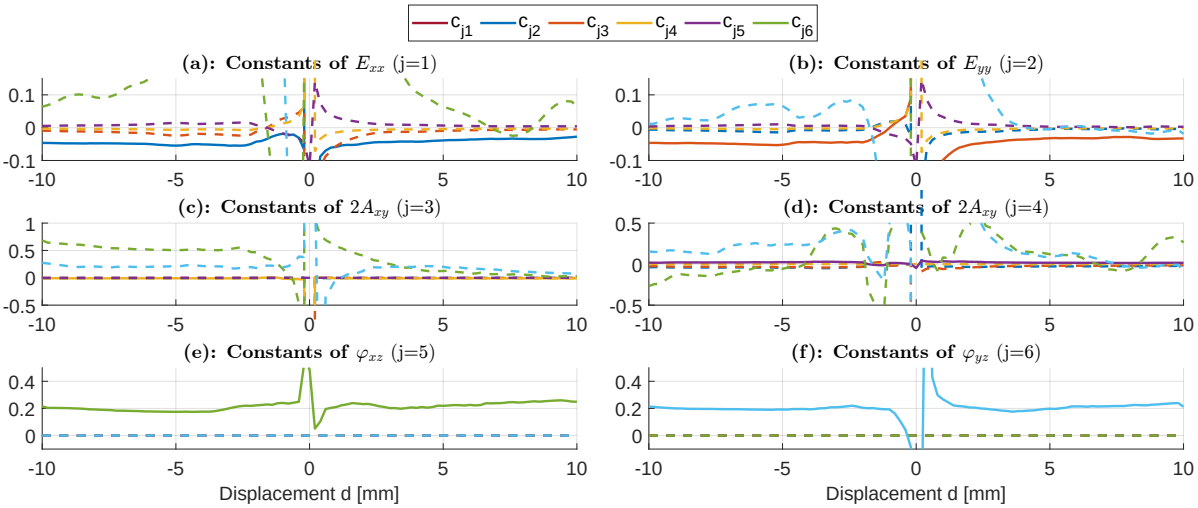

Figure 3.5: The calculated elastic constants as a function of the applied displacement d. Each plot (a-f) shows the elastic constants, related to each of the micropolar strains, E_{xx} (a), E_{yy} (b), E_{xy} (c), A_{xy} (d), φ_{xz} (e) and φ_{yz} (f). Here the sold lines represent the material moduli on the diagonal of the DME tensor, and the dashed lines represent the off-diagonals.

It should be noted that typically, the elastic constants are defined as the slope of the stress-strain curves. Here, this is impractical, as this would combine the effects of six potential micropolar constants into each stress-strain curve. Looking at **Figure 3.5** it appears that the elastic constants can be found as the asymptotes of the signal when plotted against the applied displacement. On top of this, these asymptotes show a minimal change over the applied displacement d, indicating linear elastic behavior over the entire strain range of ± 10 %.

To approximate the asymptotic value at $d = 0$, we average the elastic constants at the endpoints of the displacements curve $d = \pm 10$. An example of this asymptote for the separate rotation experiment is presented in **Figure 3.6**. This yielded the experimental entries of the DME tensor to be:

$$\begin{Bmatrix} S_{xx} \\ S_{yy} \\ S_{xy} \\ T_{xy} \\ m_{xz} \\ m_{yz} \end{Bmatrix} = \begin{bmatrix} -0.0369 & -0.0074 & -0.0029 & 0.0047 & 0.0644 & 1.0881 \\ -0.0044 & -0.0397 & -0.0020 & 0.0032 & 0.9896 & -0.0039 \\ -0.0052 & -0.0043 & -0.0097 & 0 & 0.3549 & 0.1699 \\ -0.0289 & -0.0211 & 0 & 0.0169 & -0.0025 & 0.0346 \\ 0 & 0 & 0 & 0 & 0.2321 & 0 \\ 0 & 0 & 0 & 0 & 0 & 0.2125 \end{bmatrix} \begin{Bmatrix} E_{xx} \\ E_{yy} \\ 2E_{xy} \\ 2A_{xy} \\ \varphi_{xz} \\ \varphi_{yz} \end{Bmatrix} \tag{3.1}$$

3.1.4. Internal rotation experiment

In this case, the internal rotation experiment was not required to solve the system of equations. However, it can still serve as an additional check on the derived constant by the decoupled shear experiments. **Figure 3.6** shows this separate elastic constant. From it, we derive that its value evaluated at extremity deformation to be $c_{44}^{rot} = 0.0024$. This value is very closely agrees with the value calculated in the previous section using the shear experiments.

3.2. Analytical decoupled micropolar elastic tensor

In this section, the analytical version of the DME tensor is solved for the specific geometric parameters used in this study. Only the Young's modulus and Poisson's ratio of the base material, PETG, are to be characterized still.

3.2.1. Identifying base material properties

As identified by Özen [41], the Poisson's ratio of 3D printer PETG is assumed to be $\nu = 0.35$. Regarding the Young's modulus of PETG, it was found to be highly dependent on exact printing parameters, environmental conditions and post processing [21].

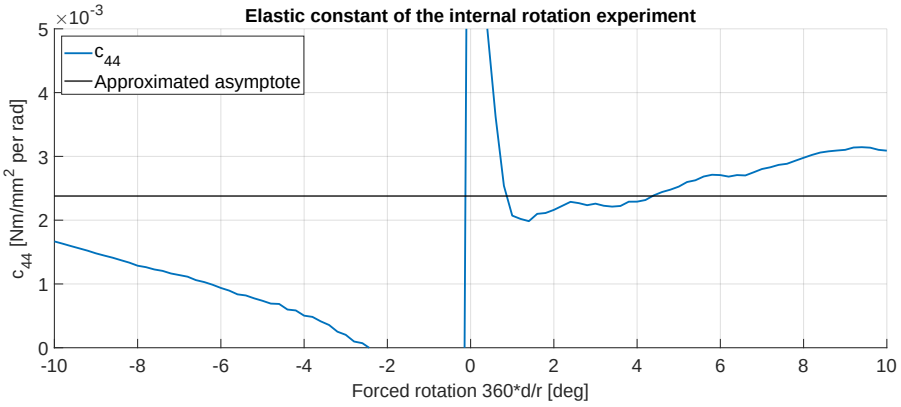

Figure 3.6: The elastic constant found by the separate internal rotation experiment as a function of the applied rotation $360 * d/r$, with r the diameter is the wire spool used in actuation. The solid black line is the asymptote that describes the elastic constant, essentially removing the effect of the singularity from the result.

For this reason, this study finds the effective Young's modulus of the 3D printed PETG by model-matching a Finite Element simulation to the observed force-displacement curve of the axial experiments. In this way, the effective Young's modulus of the base material was found to be $E_b \approx 800$ MPa, which lies well in the wide range found in literature (400 MPa - 2 GPa) and is consistent with the values found in the literature [21].

Table 3.3: Geometric parameters used for calculating the analytical micropolar constants.

Dimensionless thickness	η	0.05 [-]
Initial angle	θ_0	60 [deg]
Base Young's modulus	E_b	800 [MPa]

3.2.2. Calculating the analytical result

Using these parameters, the elastic constants are calculated to be:

$$\begin{array}{ccccccc} \mu & \lambda & \gamma & \kappa & A & B & \zeta \\ 0.0364 & 0.0364 & 0.0218 & 0.0276 & 0 & 0.0046 & 0.0333 \end{array} \tag{3.2}$$

Which can be filled into **Equation 2.16** to retrieve the values of the analytical DME tensor as:

$$\begin{Bmatrix} S_{xx} \\ S_{yy} \\ S_{xy} \\ T_{xy} \\ m_{xz} \\ m_{yz} \end{Bmatrix} = \begin{bmatrix} 0.1425 & 0.0031 & 0.0046 & 0 & 0 & 0 \\ 0.0031 & 0.1425 & -0.0046 & 0 & 0 & 0 \\ 0.0046 & -0.0046 & 0.0276 & 0 & 0 & 0 \\ 0 & 0 & 0 & 0.0124 & 0 & 0 \\ 0 & 0 & 0 & 0 & 0.0218 & 0 \\ 0 & 0 & 0 & 0 & 0 & 0.0218 \end{bmatrix} \begin{Bmatrix} E_{xx} \\ E_{yy} \\ 2E_{xy} \\ 2A_{xy} \\ \varphi_{xz} \\ \varphi_{yz} \end{Bmatrix}. \tag{3.3}$$

3.3. Comparing the elastic constants

In this section, a qualitative and quantitative comparison between the results is presented. Starting with the prediction by fourfold-symmetry q^{sym} as described in **Section 2.1.4**:

$$q^{sym} = \begin{bmatrix} c_{11} & c_{12} & c_{13} & c_{14} & 0 & 0 \\ & c_{11} & -c_{14} & -c_{13} & 0 & 0 \\ & & c_{33} & c_{34} & 0 & 0 \\ & & & c_{33} & 0 & 0 \\ & sym & & & c_{55} & 0 \\ & & & & & c_{55} \end{bmatrix} \tag{3.4}$$

And the analytical result q^{ana} as described in **Section 2.2.3**.

$$q^{ana} = \begin{bmatrix} \begin{bmatrix} 0.1425 & 0.0031 & 0.0046 & 0 \\ 0.0031 & 0.1425 & -0.0046 & 0 \\ 0.0046 & -0.0046 & 0.0276 & 0 \\ 0 & 0 & 0 & 0.0124 \end{bmatrix} & \mathbf{0} \\ \mathbf{0} & \begin{bmatrix} 0.0218 & 0 \\ 0 & 0.0218 \end{bmatrix} \end{bmatrix} \tag{3.5}$$

We see that the major symmetry of the tensor is satisfied in both cases, as expected from the assumptions in both their derivations. The principal axial stiffnesses also match, both finding that $c_{11} = c_{22}$. However, Cui's prediction that $c_{23} = -c_{14}$ and $c_{42} = -c_{13}$ does not transfer to the analytical case. Instead, it finds that $c_{23} = -c_{13}$. On top of this, the analytical model finds that $c_{14} = c_{24} = c_{34} = 0$, whereas they were predicted to be present by the predictions of Cui. Additionally, the prediction of Cui that $c_{44} = c_{33}$ does not hold in the analytical model either. Lastly, both predict the cross-coupling entries of the upper-right of the tensor are predicted to be zero in both cases, and that $c_{66} = c_{55}$. **Table 3.4** shows this comparison in a tabular format. Next, these findings are compared to the experimental results q^{exp} found in this study.

$$q^{exp} = \begin{bmatrix} \begin{bmatrix} -0.0369 & -0.0074 & -0.0029 & 0.0047 \\ -0.0044 & -0.0397 & -0.0020 & 0.0032 \\ -0.0052 & -0.0043 & -0.0097 & 0 \\ -0.0289 & -0.0211 & 0 & 0.0169 \end{bmatrix} & \begin{matrix} 0.0644 & 1.0881 \\ 0.9896 & -0.0039 \\ 0.3549 & 0.1699 \\ -0.0025 & 0.0346 \end{matrix} \\ \mathbf{0} & \begin{bmatrix} 0.2321 & 0 \\ 0 & 0.2125 \end{bmatrix} \end{bmatrix} \tag{3.6}$$

Starting off, it was found that the major symmetry in the tensor, described by both Cui [12] and Bahaloo [2], were not retrieved from these experiments. In stead, the experimentally obtained tensor q^{exp} contains many terms that differ significantly between the upper-right part of the tensor and the lower-left part of the tensor.

Moving on, we can investigate these qualitative relationships in the tensor by checking the relative strength of the predicted couplings presented above. This is detailed in **Table 3.4**.

Table 3.4: A comparison between predicted couplings by Cui [12] and by the analytical model by Bahaloo [2].

$\mathcal{C}$	$c_{22} = c_{11}$	$c_{22} = c_{11}$	$c_{22} = 1.08c_{11}$	$c_{22} = c_{11}$
	$c_{23} = -c_{14}$	$c_{23} = -c_{13}$	$c_{23} = -0.43c_{14} = 0.70c_{13}$	None
	$c_{42} = -c_{13}$	$c_{14}, c_{24} = 0$	$c_{42} = -1.1c_{13}$	$c_{42} = -c_{13}$
	$c_{34} \neq 0$	$c_{34} = 0$	$c_{34} = 0$	$c_{34} = 0$
$\mathcal{B}$	All zeros	All zeros	Fully exists	None
$\mathcal{D}$	$c_{66} = c_{55}$	$c_{66} = c_{55}$	$c_{66} = 0.92c_{55}$	$c_{66} = c_{55}$
	$c_{56} = 0$	$c_{56} = 0$	$c_{56} = 0$	$c_{56} = 0$

Based on **Table 3.4** we find that the prediction by Cui [12] and Bahaloo [2] agree on the fact that $c_{11} = c_{22}$ and that $c_{55} = c_{66}$. These findings are confirmed by our experimental results as well, and makes sense when observing that the fourfold symmetric UC is identical under 90-degree rotations. Regarding the off-diagonal c_{23}, neither of the predictions matched the experimental findings well, with either the sign or the magnitude diverging from our results. Regarding the off diagonal c_{42}, the prediction by Bahaloo matches our findings that it should not be present in the DME tensor. The off-diagonal c_{56} also matches with both predictions. Lastly, both predictions assumed that the cross-couplings contained by the $\mathcal{B}$ part of the tensor were all zeros. However, in this work they are all present with relatively strong stiffness entries compared to the other constants.

For a more quantitative comparison, we create an additional matrix. Here, the components of the analytical tensor are divided by the non-zero components of the analytical tensor element-wise. Thus retrieving their relative magnitude and making the sign differences clear.

$$q^{exp} = \begin{bmatrix} -0.2592 & -2.3835 & -0.6353 & 0 & 0 & 0 \\ -1.4277 & -0.2783 & 0.4230 & 0 & 0 & 0 \\ -1.1266 & 0.9220 & -0.3530 & 0 & 0 & 0 \\ 0 & 0 & 0 & 1.3624 & 0 & 0 \\ 0 & 0 & 0 & 0 & 10.6474 & 0 \\ 0 & 0 & 0 & 0 & 0 & 9.7454 \end{bmatrix} \odot q^{ana} \tag{3.7}$$

Here, $\odot$ denotes the element-wise multiplication symbol. Furthermore, it should be noted that this tensor does not say anything regarding the elastic constants that were not present in the analytical prediction.

Looking at these relative strengths, the diagonals of the axial elastic constants c_{11} and c_{22} were measured to be around $-1/4^{\text{th}}$ that of the analytical prediction. Off-diagonals c_{12} and c_{21} are of opposing sign and very different from the analytical results. c_{31} and c_{32} are close to the analytical values, but c_{13} is of opposite sign. On the other side, this does not hold for c_{13} and c_{23}. c_{13} is also of opposite sign compared to the analytical result, but the magnitude is much further apart. The diagonal c_{33} was found to have opposite sign and 0.35 times the magnitude compared to the analytical result. the diagonal c_{44} matches the analytical prediction reasonably well, being 36% off. The final diagonals c_{55} and c_{66} were found to be approximately 10 times stronger than predicted by the analytical model. All cross coupling terms in the upper-right of the tensor were were experimentally observed, contrary to predictions. However, the entries in the lower-left of the tensor were found to be zero, aligning with the predictions.

4

Discussion

4.1. Validity of the results

It should be noted that numerous errors in the experiments were found during the analysis. In this section, the validity of the obtained results are investigated, and the potential effects of both the errors and the assumptions made onto the DME tensor components are detailed.

Mistakes in the setup

When looking at the results presented, one of the notable observations is the significance of the hysteresis effect in the force data of all experiments as illustrated by **Figure 3.1**. This pronounced hysteresis effect arises directly from the applied grease between the base-plate slot and actuated slider. However, due to the high repeatability (all loops almost perfectly align), this hysteresis effect can effectively be removed.

Additionally, a strange phenomenon is observed. in **Figure 3.1** where the shear force, and correspondingly the measured torque, crosses itself at $d \approx 4$ mm. This insinuates that energy is not dissipated but generated in the range $4 < d < 9$ mm. The only possible explanation appears to be that the sliding friction is directionally dependent. In this case, friction term appears to vanish when the displacement passes $d > 1$mm with positive velocity. Then, once it switches direction, the sliding friction increases again, resulting in a more negative measured F_x. Unfortunately, this explanation might be insufficient, and the true origins of its occurrence are not yet understood.

Looking at the full set of force-displacement curves shown in **Appendix D** and the motion-tracked results, it was found that the shear experiments experienced a small jamming occurring at around $d = -2$ and $d = -5$mm. This was later found to stem from a manufacturing defect in the slider of the shear experiments, which bumped into the base-plate when the actuator pushed it in. This significantly affected the results and although a polynomial fit was used to remove some of its effect, the results must be interpreted with additional care. Besides this jam, some of the measurements were found to have loose boundary constraints, resulting in some parasitic deformation modes at those locations on the boundary of the sample. An overview of these observations is presented in **Appendix C**.

Taking these observations into account, it can inferred how they influenced the results. Whenever a node got stuck in the actuator, its internal rotation mode got constrained and reduced the effective bendable length of the sample, effectively increasing the strain energy density of the sample. The average internal rotation ϕ would thus become smaller, whilst the measured forces are likely larger. It should be noted that whenever one part of the UC became stuck, another appeared to show an extra pronounced deformation or rotation. This might reduce the described effect on mean rotation, but does not remove the effect on the bendable length. As such, this observation probably caused an overall increase in stiffness value for the elastic constants derived from that experiment.

On the other hand, whenever a boundary was poorly fixed, allowing a rotation to occur, the opposite happens. Due to this free rotation, moments are not transferred properly to the base-plate, reducing the torque measurement on the sensor. Additionally, the sample can achieve a more relaxed state compared to when the boundaries are fully constrained. This results in a lower strain energy of the entire sample, probably yielding lower overall stiffness values for the elastic constants derived from that experiment.

Influence of assumptions

Besides these anomalies in the experiments, the assumptions made on how the reaction forces contribute to the stress components and what strain components were assumed to be zero also impact the findings.

Regarding the stress definitions, it was found that the choice of sign in the reaction forces causes some diagonal entries of the elastic tensor to be negative. E.g. under a negative displacement d, some reaction forces are positive. As such, we divide a negative stress over positive strain, or vise versa, resulting in negative elastic constants. Additionally, the couple stress terms are set to zero by definition, except for the bending experiments. The experimental setup implemented in this study was unable distinguish between the moments applied on each face independently. Therefore, all moment contributions were allocated to the internal rotation. Future work might include a torque sensor on each constraint.

Moving on to the strain assumptions, we can predict their influence from a strain energy density perspective. By setting some strains to be zero, the stresses they might have induced are reallocated to the remaining strains. Therefore, the remaining strains show an even more pronounced elastic constants, as the observed reaction forces, which are a direct result from the strain energy of the deformed sample, remain unchanged.

4.2. Interpreting the decoupled micropolar elastic tensors

To begin, we found that the derived elastic constants remain relatively constant over a 10 percent strain range, thus supporting the use of linear approximations in the analysis of these materials.

Moving on to the experimentally obtained DME tensor, it should be noted that the diagonal constants should be positive definite, as the total strain energy must be positive definite. This indicates sign-mistakes in derivations, probably arising from an inverted definition of the positive direction between the actuator axes, sensor axes and/or motion-tracked axes. However, the specific source of this error could not be identified.

Looking at the axial diagonal elastic constants c_{11} and c_{22}, their magnitude was found to be smaller than the analytical prediction. It was also found that the internal rotations were found to play a significant role in axial deformations. From a strain energy perspective, this means that a portion the strain energy ascribed to the axial elastic constants c_{11} and c_{22} could have been transferred to the strain energy carried by the internal rotation related constants c_{41} and c_{42}. This effect is not present in the analytical model, and for that reason could have caused this weakening of the diagonal. Additionally, the couplings between internal rotation and principal strains c_{14}, c_{24} support the idea that overall dilation stiffness is driven by the internal rotation of such MMs, which was suggested by various other studies [35, 59].

Regarding the diagonal constants c_{55} and c_{66}, the opposite effect was observed, being significantly stronger compared to the analytical prediction yet equal to each other from the experiments. This discrepancy deserves further investigation, but is not explored further in this study.

Next, the major symmetries of the off-diagonal entries can be investigated. Here, a significant difference in magnitude between ”opposite” constants c_{ij} and c_{ji} was observed, possibly arising from the separation of experiments with which the constants are measured, and the culmination of assumptions and errors in the measurements. However, these differences are still quite large with respect to, for example the axial constants c_{11}/c_{22} and the curvature constants c_{55}/c_{66} which are both within 10% of magnitude. As such, our work supports the idea that the major symmetries are not necessarily satisfied in the micropolar tensor, indicating anisotropic behavior [11].

On the other hand, the tensor asymmetry in the cross-coupling constants, from c_{15} to c_{46} compared to c_{51} to c_{64}, directly follows from the assumptions made on the measured couple-stresses. A couple-stress existing as a reaction force would have to be equal and opposite on both attachments to the base-plate. Thus making it impossible to measure when utilizing just one reaction-force sensor. Their presence could only be assumed for bending experiments, and it is unclear to what extend these couple-stresses might influence in the other experiments executed in this study. However, the upper-right part of the tensor, from c_{15} to c_{46}, was fully filled.

All of these constants were predicted to be zero through both the analytical model and the symmetry predictions. Yet, in our experiments they all show a strong presence in magnitude. This suggests that the curvature strains introduce large stresses in all aspects of the decoupled micropolar description. The results found here are hard to validate, as this section of the tensor is often set to zero by assumption in the micropolar models. Nevertheless, the results obtained in this cross-coupling part of the tensor do seem legitimate when taking into account the compressibility of the internal structures. Thus, when performing bending experiments, a principal strain perpendicular to the axis of curvature is induced, which in-turn corresponds strongly with the symmetric- and antisymmetric shear strains. Furthermore, during the experiments, there appeared to be a transition-area. In the upper half of the sample, the actuated side, shear and internal rotation appeared dominant under the applied strain. On the bottom half of the sample, the curvature strain took the upper hand. This effect is visualized in **Figure A.1b**. This peculiar separation of strains throughout the height of the sample is something to look into more, but will not be discussed further here.

4.3. Relevance to the field

Looking at the analytical model of [2], it was noted that $\mathcal{B}$ only vanishes as a result of assumed isotropy in [35] and hemitropy in [10]. These studies compensate for this simplification by adding additional parameters in the $\mathcal{C}$ part of the constitutive relation to reintergrate anisotropy and chirality into the constitutive relation. Using these additional parameters, Bahaloo creates a V-beam finite element to reduce nodal DOFs and derive analytical solutions for a planar chiral lattice. [2], which is then used by [34] to show that the Mr4 geometry is highly anisotropic. Unfortunately, generalization of this analytical model is difficult as the derivation of the stiffness matrices proved tedious and highly dependent on unit-cell geometry.

As such, there now appears to be a circular logic. Initially, full isotropy or hemitropy is assumed, forcing the micropolar tensor to be symmetric and setting the cross-coupling matrix $\mathcal{B} = \mathbf{0}$. Then, additional elastic constants have to be introduced to accurately describe the material behavior based on chirality and anisotropy. In reality, it was found that the micropolar elastic tensor does not require the major symmetries to be present [11]. While isotropic assumptions have been found to translate to anisotropic media from the perspective of bounded elastic properties[3], we find that their deformation behavior is still fundamentally different from the perspective of the DME tensor. As such, it might concluded that it is the asymmetry and cross-coupling terms of in the DME tensor that are the most descriptive of the unique behaviors present inside MMs, warranting further investigation.

Performing these experiments with FE methods might prove to be more convenient; however there remains the same problem of measuring the couple-stresses. Here, more complex FEM models should be implemented that are capable to extract reaction moments on each part of the constraint faces, such that it can always be related to a couple stress.

In literature regarding micropolar elasticity, the micropolar elastic constants are used for the constitutive framework. However, in this work, we were unable to relate the entries of the DME tensor c_{ij} to the micropolar elastic constants λ, μ, κ and γ or to the engineering constants E_m, ν_m, l and N. This stems from the isotropic assumption used in the definition of the material constants. Based on Eringen [17], a fully anisotropic thermo-elastic solid can have up to 196 independent material moduli. These have been simplified towards the creation of linear isotropic and centrosymmetric material models [17], but such work is yet to be implemented in materials that exhibit anisotropic and non-centrosymmetric behavior.

4.4. Generalization

In this work, only one tetra-chiral geometry is analyzed. Yet, we were unsuccessful in fully validating the observed results with existing literature. Perhaps our method is flawed, or perhaps there is something missing in literature. In future work, a more fine-tuned version of the method could be implemented to yield more reliable and higher-accuracy measurements of the micropolar material moduli. With this, comparisons with analytical models could be made with more certainty. Furthermore, the influence of symmetry, chirality and hierarchy could all be investigated with the proposed method. Here, the proposed method for sample-scaling might allow fairer comparisons with respect to analytical literature, especially when investigating the scale-ability of the MM material moduli.

Taking another step back, this work only begins to explore the surface of the continuum models used for describing MMs. Other descriptions might still prove effective to fully describe the spectra of possible behaviors in MMs. However, more research is needed to make any meaningful claims regarding differences in effectiveness between the continuum descriptions and the assumptions made in them.

On another note, research suggests that micropolar descriptions of MMs do not scale [5, 11]. This is an interesting finding and deserves to be investigated further. Does it still hold when scaling non-dimensional parameters that define the stiffness like in this work? Or is it that the characteristic length used in micropolar elasticity does not scale proportional to the unit-cell length? Or are these findings artifacts from isotropic assumptions on the tensor? Moreover, future work could explore how not just scale, but hierarchy influences the observed behavior, through stacking UCs of varying sizes, or grouping various UCs into higher-order repeating patterns.

5

Conclusion

In this work, we identify DME theory as a suitable framework for more extensive analysis of chiral MMs. A two-dimensional simplification of the theory was applied to synthesize an experimental method capable of measuring all micropolar elastic constants without relying on preliminary assumptions frequently applied in the literature. A specific family of planar chiral metamaterials, the Missing Rib 4 geometry, is investigated. Through our proposed methodology, we find the values of 36 potential independent micropolar elastic constants. The results are compared to state-of-the-art analytical models, and symmetry-based predictions.

It was found that all three decoupled micropolar tensors show differing results. The analytical model does not predict independent couplings between internal micro-rotations of a micropolar continuum, whereas these are predicted from symmetry. Our analytical results agreed with both predictions regarding the diagonal constants related to axial strains and regarding the curvatures. For the off-diagonal terms, no consistent agreement was found between the various predictions and the obtained results.

Additionally, our results show relatively strong coupling effects in the elastic constants between micropolar curvatures and all corresponding micropolar stresses components. This result differs from most existing literature, where such couplings are often assumed zero in the face of isotropy. As such, it appears that the assumption of isotropy might not be a suitable assumption in the analysis of MMs, and that more research is needed to find the elastic constants of anisotropic MMs. Besides these cross-couplings in the elastic tensor, the internal rotations showed coupled behavior to the axial strains, supporting the thought that the dilatation stiffness of these compressible materials is influenced by their capacity to have internal rotations.

On top of these results, this study found that all decoupled micropolar elastic constants showed consistent values over a strain range of $\pm 10\%$. This supports the use of linear-elasticity-based assumptions in the analysis of MMs. Yet, more research is needed to investigate how this finding scales with tessellation size (number of UCs) and UC size.

All in all, proper validation of the observed elastic constants remains challenging due to assumptions in the literature that may not be universally valid when applied to chiral mechanical metamaterials. Additionally, there appears to be a general scarcity of experimental validations of micropolar elastic tensors, especially for anisotropic cases. Moving forward, further development of these theories may be essential for the development of more rigorous bridges between MM geometry and functional behavior.

References

[1] A. Bacigalupo et al. “Overall constitutive properties of stratified lattices with alternating chirality”. In: *Philosophical Transactions A* 382.2279 (Aug. 2024). ISSN: 1364503X. DOI: 10.1098/RSTA.2023.0355.

[2] H. Bahaloo and Y. Li. “Micropolar Modeling of Auxetic Chiral Lattices with Tunable Internal Rotation”. In: *Journal of Applied Mechanics, Transactions ASME* 86.4 (Apr. 2019). ISSN: 15289036. DOI: 10.1115/1.4042428/446426.

[3] J.B. Berger, H.N.G. Wadley, and R.M. McMeeking. “Mechanical metamaterials at the theoretical limit of isotropic elastic stiffness”. In: *Nature* 543.7646 (Mar. 2017), pp. 533–537. ISSN: 14764687. DOI: 10.1038/NATURE21075.

[4] K. Bertoldi et al. “Flexible mechanical metamaterials”. In: *Nature Reviews Materials 2017 2:11* 2.11 (Oct. 2017), pp. 1–11. ISSN: 2058-8437. DOI: 10.1038/natrevmats.2017.66.

[5] A.J. Beveridge, M.A. Wheel, and D.H. Nash. “The micropolar elastic behaviour of model macroscopically heterogeneous materials”. In: *International Journal of Solids and Structures* 50.1 (Jan. 2013), pp. 246–255. ISSN: 0020-7683. DOI: 10.1016/J.IJSOLSTR.2012.09.023.

[6] M.H. Bloembergen. “Thermally Programmable Multi-stable Mechanical Metamaterial”. PhD thesis. TU Delft, 2025. URL: https://repository.tudelft.nl/record/uuid:9cf8f612-5b0d-4823-81e5-2388e8f60f32.

[7] A.L. Cauchy. “Mémoire sur les systèmes isotropes de points materiels”. In: *Mém. Acad. Sci.* 22 (1850), p. 615.

[8] J. Charmant and contributors. *Kinovea (2023. 1.2)*. 2024. URL: https://www.kinovea.org.

[9] J. Chen et al. “A one-dimensional model for mechanical coupling metamaterials using couple stress theory”. In: *Mathematics and Mechanics of Solids* 28.12 (Dec. 2023), pp. 2732–2755. ISSN: 17413028. DOI: 10.1177/10812865231177670.

[10] Y. Chen et al. “Micropolar continuum modelling of bi-dimensional tetrachiral lattices”. In: *Proceedings of the Royal Society A: Mathematical, Physical and Engineering Sciences* 470.2165 (May 2014). ISSN: 14712946. DOI: 10.1098/RSPA.2013.0734.

[11] R. Craster et al. “Mechanical metamaterials”. In: *Reports on Progress in Physics* 86.9 (Aug. 2023), p. 094501. ISSN: 0034-4885. DOI: 10.1088/1361-6633/ACE069.

[12] Z. Cui and J. Ju. “Mechanical coupling effects of 2D lattices uncovered by decoupled micropolar elasticity tensor and symmetry operation”. In: *Journal of the Mechanics and Physics of Solids* 167 (2022), p. 105012. DOI: 10.1016/j.jmps.2022.105012.

[13] Z.M. Cui, Z.H. Yuan, and J.H. Ju. “Mechanical Couplings of 3D Lattice Materials Discovered by Micropolar Elasticity and Geometric Symmetry”. In: *Journal of the Mechanics and Physics of Solids* 90.4 (2023), p. 041001. DOI: 10.1115/1.4056349.

[14] K.K. Dudek et al. “Shape Morphing Metamaterials”. In: *arXiv* 2501.14804 (Jan. 2025).

[15] E. Cosserat and F. Cosserat. “Théorie des Corps déformables”. In: *Nature 1909 81:2072* 81.2072 (July 1909), pp. 67–67. ISSN: 1476-4687. DOI: 10.1038/081067a0.

[16] A. Cemal Eringen. “Linear Theory of Micropolar Elasticity”. In: *Journal of Mathematics and Mechanics* 15.6 (1966), pp. 909–923.

[17] A. Cemal Eringen. “Theory of Micropolar Elasticity”. In: *Microcontinuum Field Theories*. Springer New York, 1999. DOI: 10.1007/978-1-4612-0555-5.

[18] S. Eskandari, B. shahryari, and A. Akbarzadeh. “Unravelling Size-Dependent and Coupled Properties in Mechanical Metamaterials: A Couple-Stress Theory Perspective”. In: *Advanced Science* 11.13 (Apr. 2024), p. 2305113. ISSN: 2198-3844. DOI: 10.1002/ADVS.202305113.

[19] H.B. Fang et al. “Origami lattices and folding-induced lattice transformations”. In: *Physical Review Research* 1.2 (2019), p. 023010. DOI: 10.1103/PhysRevResearch.1.023010.

[20] J. Gao et al. “Rational designs of mechanical metamaterials: Formulations, architectures, tessellations and prospects”. In: *Materials Science and Engineering: R: Reports* 156 (2023), p. 100755. DOI: 10.1016/j.mser.2023.100755.

[21] S. Guessasma, S. Belhabib, and H. Nouri. “Printability and Tensile Performance of 3D Printed Polyethylene Terephthalate Glycol Using Fused Deposition Modelling”. In: *Polymers 2019, Vol. 11, Page 1220* 11.7 (July 2019), p. 1220. ISSN: 2073-4360. DOI: 10.3390/POLYM11071220.

[22] S. Hassanpour and G.R. Heppler. “Micropolar elasticity theory: A survey of linear isotropic equations, representative notations, and experimental investigations”. In: *Mathematics and Mechanics of Solids* 22.2 (Feb. 2017), pp. 224–242. ISSN: 17413028. DOI: 10.1177/1081286515581183.

[23] S. Hassanpour and G.R. Heppler. “Step-by-Step Simplification of the Micropolar Elasticity Theory to the Couple-Stress and Classical Elasticity Theories”. In: *ASME International Mechanical Engineering Congress and Exposition, Proceedings (IMECE)* 9 (Mar. 2015). DOI: 10.1115/IMECE2014-39216.

[24] A. Hasse and K. Mauser. “Poisson Induced Bending Actuator for Soft Robotic Systems”. In: *Soft Robotics* 7.2 (Apr. 2020), pp. 155–167. ISSN: 21695180. DOI: 10.1089/SORO.2018.0163,.

[25] J.B. Hopkins and R.M. Panas. “Design of flexure-based precision transmission mechanisms using screw theory”. In: *Precision Engineering* 37.2 (Apr. 2013), pp. 299–307. ISSN: 0141-6359. DOI: 10.1016/J.PRECISIONENG.2012.09.008.

[26] S.F. Iftekar et al. “Advancements and Limitations in 3D Printing Materials and Technologies: A Critical Review”. In: *Polymers 2023, Vol. 15, Page 2519* 15.11 (May 2023), p. 2519. ISSN: 2073-4360. DOI: 10.3390/POLYM15112519.

[27] Y. Jiang and Y. Li. “3D Printed Auxetic Mechanical Metamaterial with Chiral Cells and Re-entrant Cores”. In: *Scientific Reports* 8.1 (Dec. 2018), pp. 1–11. ISSN: 20452322. DOI: 10.1038/s41598-018-20795-2.

[28] JPE-innovations. *Precision Point - JPE*. Accessed on 13.05.2025. URL: https://www.jpe-innovations.com/precision-point/.

[29] W.T. Koiter. “Couple Stresses in the Theory of Elasticity, I and II.” In: *Proceedings Series B, Koninklijke Nederlandse Akademie van Wetenschappen*. Koninklijke Nederlandse Akademie van Wetenschappen, 1969, pp. 17–44.

[30] H.M.A. Kolken et al. “Rationally designed meta-implants: a combination of auxetic and conventional meta-biomaterials”. In: *Materials Horizons* 5.1 (Jan. 2018), pp. 28–35. ISSN: 20516355. DOI: 10.1039/C7MH00699C.

[31] R.S. Lakes. “Experimental microelasticity of two porous solids”. In: *International Journal of Solids and Structures* 22.1 (Jan. 1986), pp. 55–63. ISSN: 0020-7683. DOI: 10.1016/0020-7683(86)90103-4.

[32] R.S. Lakes. “Size effects and micromechanics of a porous solid”. In: *Journal of Materials Science* 18.9 (Sept. 1983), pp. 2572–2580. ISSN: 00222461. DOI: 10.1007/BF00547573/METRICS.

[33] T. Li and Y. Li. “Mechanical behaviors of three-dimensional chiral mechanical metamaterials”. In: *Composites Part B: Engineering* 270 (Feb. 2024), p. 111141. ISSN: 1359-8368. DOI: 10.1016/J.COMPOSITESB.2023.111141.

[34] T. Li and Y. Li. “Prediction of the Anisotropy of Chiral Mechanical Metamaterials via Micropolar Modeling”. In: *Journal of Applied Mechanics, Transactions ASME* 89.10 (Oct. 2022). ISSN: 15289036. DOI: 10.1115/1.4055349/1145709.

[35] X. N. Liu, G.L. Huang, and G.K. Hu. “Chiral effect in plane isotropic micropolar elasticity and its application to chiral lattices”. In: *Journal of the Mechanics and Physics of Solids* 60.11 (Nov. 2012), pp. 1907–1921. ISSN: 0022-5096. DOI: 10.1016/J.JMPS.2012.06.008.

[36] B. McCarthy et al. “Design of configuration indifferent compliant building blocks”. In: *Precision Engineering* 81 (May 2023), pp. 60–67. ISSN: 0141-6359. DOI: 10.1016/J.PRECISIONENG.2023.02.002.

[37] R. D. Mindlin and H. F. Tiersten. “Effects of couple-stresses in linear elasticity”. In: *Archive for Rational Mechanics and Analysis* 11.1 (Jan. 1962), pp. 415–448. ISSN: 00039527. DOI: 10.1007/BF00253946/METRICS.

[38] S. Nakamura and R.S. Lakesi. “Finite element analysis of saint-venant end effects in micropolar elastic solids”. In: *Engineering Computations* 12.6 (June 1995), pp. 571–587. ISSN: 02644401. DOI: 10.1108/02644409510799785/FULL/PDF.

[39] H. Nassar and P. Brucks. “Willis elasticity from microcontinuum field theories: Asymptotics, microstructure - property relationships, and cloaking”. In: *Wave Motion* 122 (2023). DOI: 10.1016/j.wavemoti.2023.103206.

[40] J.T.B. Overvelde et al. “Rational design of reconfigurable prismatic architected materials”. In: *NATURE* 541.7637 (2017), pp. 347–352. DOI: 10.1038/nature20824.

[41] A. Özen et al. “Investigation of deformation behavior of PETG-FDM-printed metamaterials with pantographic substructures based on different slicing strategies”. In: *Composites and Advanced Materials* 30 (2021). ISSN: 2634-9833. DOI: 10.1177/26349833211016477.

[42] S.K. Patiballa and G. Krishnan. “A Sequential two-step design framework for deformable mechanical metamaterials”. In: *ASME International Mechanical Engineering Congress and Exposition, Proceedings (IMECE)* 12 (2020), V012T12A022. DOI: 10.1115/IMECE2020-24270.

[43] S.K. Patiballa and G. Krishnan. “On the design of three-dimensional mechanical metamaterials using load flow visualization”. In: *Mechanics Based Design of Structures and Machines* 50.2 (2022), pp. 442–467. DOI: 10.1080/15397734.2020.1719506.

[44] S.K. Patiballa and G. Krishnan. “Qualitative analysis and conceptual design of planar metamaterials with negative Poisson’s ratio”. In: *Journal of Mechanisms and Robotics* 10.2 (2018), p. 021006. DOI: 10.1115/1.4038977.

[45] J.M. Podestá et al. “Symmetry considerations for topology design in the elastic inverse homogenization problem”. In: *Journal of the Mechanics and Physics of Solids* 128 (July 2019), pp. 54–78. ISSN: 0022-5096. DOI: 10.1016/J.JMPS.2019.03.018.

[46] S. Pyo and K. Park. “Mechanical Metamaterials for Sensor and Actuator Applications”. In: *International Journal of Precision Engineering and Manufacturing - Green Technology* 11.1 (2024), pp. 291–320. DOI: 10.1007/s40684-023-00549-w.

[47] Z. Qiu. “A Simple Theory of Asymmetric Linear Elasticity”. In: *World Journal of Mechanics* 10.10 (Oct. 2020), pp. 166–185. ISSN: 2160-049X. DOI: 10.4236/WJM.2020.1010012.

[48] P. Roberjot and J.L. Herder. “A unified design method for 2D auxetic metamaterials based on a minimal auxetic structure”. In: *International Journal of Solids and Structures* 295 (2024), p. 112777. DOI: 10.1016/j.ijsolstr.2024.112777.

[49] S.E. Rodríguez et al. “Mechanical metamaterial systems as transformation mechanisms”. In: *Extreme Mechanics Letters* 61 (June 2023), p. 101985. DOI: 10.1016/j.eml.2023.101985.

[50] W.F. dos Santos et al. “Analysis of a novel 3D-printed mechanical metamaterial with tension-induced undulation: Experimental and numerical investigations”. In: *International Journal of Solids and Structures* 317 (July 2025), p. 113402. ISSN: 0020-7683. DOI: 10.1016/J.IJSOLSTR.2025.113402.

[51] L.H. Schattenberg. “Metamaterial Behaviour for Motion Systems Using an Approximated Ideal Shear Cell”. PhD thesis. TU Delft, 2024. URL: https://repository.tudelft.nl/record/uuid:933daeb2-0fd7-442d-9487-e48b2ab82ef7.

[52] J.H. Song et al. “Artificial Intelligence in the Design of Innovative Metamaterials: A Comprehensive Review”. In: *International Journal of Precision Engineering and Manufacturing* 25.1 (2024), pp. 225–244. DOI: 10.1007/s12541-023-00857-w.

[53] R.A. Toupin. “Theories of elasticity with couple-stress”. In: *Archive for Rational Mechanics and Analysis* 17.2 (Jan. 1964), pp. 85–112. ISSN: 00039527. DOI: 10.1007/BF00253050/METRICS.

[54] R. Van Mastrigt, C. Coulais, and M. Van Hecke. “Emergent nonlocal combinatorial design rules for multimodal metamaterials”. In: *Physical Review E* 108.6 (2023), p. 065002. DOI: 10.1103/PhysRevE.108.065002.

[55] S.P. Vasudevan and P.P. Pratapa. “Homogenization of non-rigid origami metamaterials as Kirchhoff–Love plates”. In: *International Journal of Solids and Structures* 300 (Aug. 2024), p. 112929. ISSN: 0020-7683. DOI: 10.1016/J.IJSOLSTR.2024.112929.

[56] W. Voigt. “Theoretische Studien über die Elasticitätsverhältnisse der Krystalle. I.” In: *Abhandlungen der Königlichen Gesellschaft der Wissenschaften in Göttingen* 34 (1887), pp. 3–52.

[57] J.R. Willis. “Dynamics of Composites”. In: *Continuum Micromechanics* (1997), pp. 265–290. ISSN: 2309-3706. DOI: 10.1007/978-3-7091-2662-2_5.

[58] N. Yang and J.L. Silverberg. “Decoupling local mechanics from large-scale structure in modular metamaterials”. In: *Proceedings of the National Academy of Sciences of the United States of America* 114.14 (2017), pp. 3590–3595. DOI: 10.1073/pnas.1620714114.

[59] X. Yu et al. “Mechanical metamaterials associated with stiffness, rigidity and compressibility: A brief review”. In: *Progress in Materials Science* 94 (2018), pp. 114–173. DOI: 10.1016/j.pmatsci.2017.12.003.

[60] Z. Zhai, L. Wu, and H. Jiang. “Mechanical metamaterials based on origami and kirigami”. In: *Applied Physics Reviews* 8.4 (2021), p. 041319. DOI: 10.1063/5.0051088.

Epilogue

The future of mechanical metamaterials appears bright. Research on the topic is booming, yet many obstacles are still to be overcome. Most of all, generalizations to three dimensions have to be made.

Extending our work to 3D MMs would require expanding the current methodology. The symmetry predictions and DME tensor have already been expanded to 3D [13], as has the analytical model of Missing Rib 4 geometry been expanded into a so-called metacube [33]. However, a comprehensive classification does not yet exist as rigorous as has been achieved for 2D geometries by Roberjot [48].

Besides these frameworks, the experimental method for three-dimensional MMs would have to change. The traditional measurement options of the bending-creep and tensile-torsion tests become accessible again, but it remains unclear whether they are sufficient for fully anisotropic versions of DME. Alternatively, the proposed method can be expanded to the third dimension as well, but the main difficulty would reside in the quantification of strains internal to the material, as they are obstructed by the external surfaces. However, inspiration could be drawn from work by Beveridge [5].

An inverse homogenization method has been derived for Cauchy elasticity based on the point groups of two-dimensional mechanical metamaterials [45]. This could be expanded to an inverse homogenization of micropolar elasticity, but first a consensus has to be achieved regarding what parts of the tensor exist in the varying point groups of planar mechanical metamaterials. An improved version of our method might support these investigations by providing an assumption-free analysis on the existence of DME tensor components.

A micropolar extension of such an inverse homogenization method would consist of a database of three-dimensional UCs that have elastic tensors predicted by their geometric parameters and their point groups. Then, these could be tuned to contain a desired micropolar elastic tensor.

This train of thought could facilitate a so called hierarchical design framework that separates global topology, high-order repeating patterns, and the individual UCs to find an optimal geometry for a target shape-change, similar to the proposed design rules of Dudek [14]. They separate the design of MMs of moving systems into two parts: defining the design space including physical constraints, and solving computational optimization problem [14]. Here, the optimization problem might be reduced in complexity through the use of the inverse homogenization of the micropolar elastic tensors at the UC level of the framework.

Lastly, more advanced UC's could be incorporated, like the so-called building blocks based on the Freedom- and Constraint Topology of Hopkins [25]. They created building blocks that could serve as UC's, such that they do not lose their individual degrees of freedom when tessellated in any manner [36]. It would be interesting to see whether these building blocks could be described properly by micropolar continuum elements. As such, we might end up with a universal database of UC geometries and how each of its geometric parameters influences their micropolar tensor. The global elastic tensor could then be retrieved using FE techniques of assembling local elastic tensors.

All in all, the field of mechanical metamaterials is rapidly progressing. We are far from solving the quintessential question of rigorously relating the archived structures to desired shape-change or mechanism-like functionality. And perhaps, this can only be achieved through integrating expanded theories of elasticity, essentially allowing ourselves to say: *Micromotions Matter*.

A

Deriving stress components.

In this appendix the decoupled micropolar stress components are derived from the reactions forces on the constrained face of the sample.

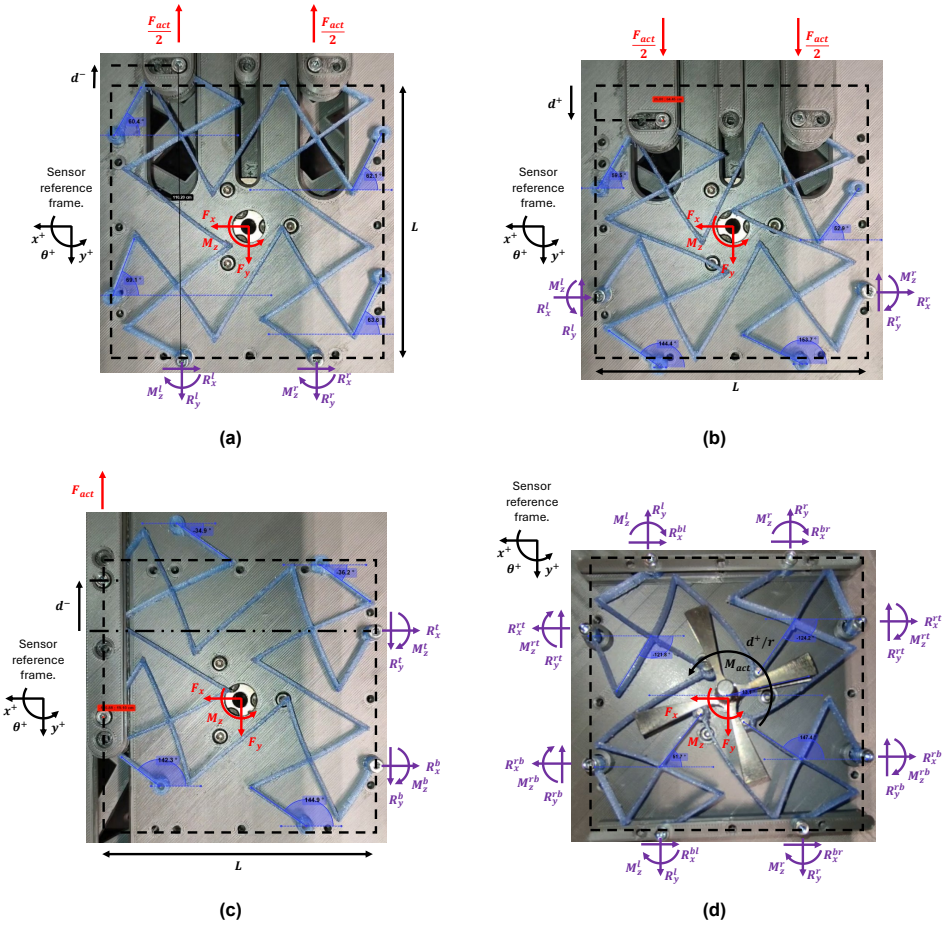

Figure A.1: Representative displacement fields of (a) the axial experiments, (b) the bending experiments, (c) the shear experiments and (d) the rotation experiments.

A.1. Axial equilibrium

For the axial experiments, shown in **Figure A.1a**, the micropolar stresses on each face are defined as:

$$\boldsymbol{S^{A1}} = \begin{Bmatrix} S_{xx} = (R_y^l + R_y^r)/Area \\ S_{yy} = 0 \\ S_{xy} = (R_x^l + R_x^r)/Area \\ T_{xy} = (M_z^l + M_z^r)/Area \\ m_{xz} = 0 \\ m_{yz} = 0 \end{Bmatrix} \quad \& \quad \boldsymbol{S^{A2}} = \begin{Bmatrix} S_{xx} = 0 \\ S_{yy} = (R_y^l + R_y^r)/Area \\ S_{xy} = (R_x^l + R_x^r)/Area \\ T_{xy} = (M_z^l + M_z^r)/Area \\ m_{xz} = 0 \\ m_{yz} = 0 \end{Bmatrix} \tag{A.1}$$

Then, the static equilibrium equations between the sensor and MM sample are found to be:

$$\sum F_{x^+} = F_x - (R_x^l + R_x^r) = 0 \tag{A.2a}$$

$$\sum F_{y^+} = F_y + (R_y^l + R_y^r) = 0 \tag{A.2b}$$

$$\sum M_O = M_z - (M_x^l + M_z^r) + \frac{L}{2}(R_x^l + R_x^r) + \frac{L}{4}(R_y^l - R_y^r) = 0 \tag{A.2c}$$

And that

$$\begin{matrix} F_x = (R_x^l + R_x^r) \\ F_y = -(R_y^l + R_y^r) \\ M_z = (M_x^l + M_z^r) - \frac{L}{2}(R_x^l + R_x^r) - \frac{L}{4}(R_y^l - R_y^r) \end{matrix} \tag{A.3}$$

Here, the load is applied in alignment with the measured principle strain. As such, S_{xx} is measured in the uni-axial in x experiment, whereas S_{yy} is measured in the uni-axial in y experiment.

By substituting the decoupled micropolar stress definitions of **Equation A.1**, these equations can be rewritten to find how the micropolar stresses appear as a function of the measured reaction loads F_x, F_y and M_z. Last, when assuming the two fixed ends of the MM sample (left and right) are loaded equally such that $R_y^l = R_y^r$, these functions become

$$\boldsymbol{S^{A1}}: \begin{matrix} S_{xx} = -F_y/Area \\ S_{xy} = F_x/Area \\ T_{xy} = \frac{M_z}{Area} - \frac{L}{2}F_x/Area \end{matrix} \quad \& \quad \boldsymbol{S^{A1}}: \begin{matrix} S_{yy} = -F_y/Area \\ S_{xy} = F_x/Area \\ T_{xy} = \frac{M_z}{Area} - \frac{L}{2}F_x/Area \end{matrix} \tag{A.4}$$

For the uni-axial in x experiment and switches $S_{xx} = 0$, $S_{yy} = -F_y/Area$ for the uni-axial in y experiment.

A.2. Bending equilibrium

For the bending experiments, shown in **Figure A.1b**, the micropolar stresses on each face are defined to be.

$$\boldsymbol{S^{B1}} = \begin{Bmatrix} S_{xx} = 0 \\ S_{yy} = (R_y^l + R_y^r)/Area \\ S_{xy} = (R_x^l + R_x^r)/Area \\ T_{xy} = (M_z^l - M_z^r)/Area \\ m_{xz} = L * (R_y^l + R_y^r)/Area \\ m_{yz} = 0 \end{Bmatrix} \quad \& \quad \boldsymbol{S^{B1}} = \begin{Bmatrix} S_{xx} = (R_y^l + R_y^r)/Area \\ S_{yy} = 0 \\ S_{xy} = (R_x^l + R_x^r)/Area \\ T_{xy} = (M_z^l - M_z^r)/Area \\ m_{xz} = 0 \\ m_{yz} = L * (R_y^l + R_y^r)/Area \end{Bmatrix} \tag{A.5}$$

Here, the load is applied perpendicular to the axis over which the curvature is measured. As such, in the Bending over x experiment (measuring φ_{xz}), the actuated load is measured in S_{yy}, which changes to S_{xx} for the Bending of y experiment (measuring φ_{yz}). Then, the static equilibrium equations between the sensor and MM sample are found to be:

$$\sum F_{x^+} = F_x - (R_x^l + R_x^r) = 0 \tag{A.6a}$$

$$\sum F_{y^+} = F_y - (R_y^l + R_y^r) = 0 \tag{A.6b}$$

$$\sum M_O = M_z + (M_x^l - M_z^r) + \frac{L}{4}(R_x^l + R_x^r) + \frac{L}{2}(R_y^r - R_y^l) = 0 \tag{A.6c}$$

And that

$$\begin{array}{c} F_x = (R_x^l + R_x^r) \\ F_y = -(R_y^l + R_y^r) \\ M_z = (M_x^l + M_z^r) - \frac{L}{2}(R_x^l + R_x^r) - \frac{L}{4}(R_y^l - R_y^r) \end{array} \tag{A.7}$$

By substituting the decoupled micropolar stress definitions of **Equation A.5**, these equations can be rewritten to find how the micropolar stresses appear as a function of the measured reaction loads F_x, F_y and M_z. Last, when assuming the two fixed ends of the MM sample (left and right) are loaded equally such that $R_y^l = R_y^r$, these functions become:

$$\boldsymbol{S^{B1}}: \begin{array}{c} S_{yy} = F_y/Area \\ S_{xy} = F_x/Area \\ T_{xy} = M_z/Area - \frac{L}{4}F_x/Area \\ m_{xz} = L * F_y/Area \end{array} \quad \& \quad \boldsymbol{S^{B2}}: \begin{array}{c} S_{xx} = F_y/Area \\ S_{xy} = F_x/Area \\ T_{xy} = M_z/Area - \frac{L}{4}F_x/Area \\ m_{yz} = L * F_y/Area \end{array} \tag{A.8}$$

A.3. Shear equilibrium

A.3.1. Deriving decoupled micropolar stresses.

Assuming a standard micropolar stress tensors for shear on x $S1$ and shear on y $S2$ respectively as:

$$\boldsymbol{\sigma^{S1}} = \begin{Bmatrix} \sigma_{xx} = (R_x^t + R_x^b)/Area \\ \sigma_{yy} = 0 \\ \sigma_{xy} = \frac{(R_y^t + R_y^b)}{Area} - \frac{(M_z^t + M_z^b)}{Area} \\ \sigma_{yx} = \frac{(M_z^t + M_z^b)}{Area} \\ m_{xz} = 0 \\ m_{yz} = 0 \end{Bmatrix} \quad \& \quad \boldsymbol{\sigma^{S2}} = \begin{Bmatrix} \sigma_{xx} = 0 \\ \sigma_{yy} = (R_x^t + R_x^b)/Area \\ \sigma_{xy} = \frac{(M_z^t + M_z^b)}{Area} \\ \sigma_{yx} = \frac{(R_y^t + R_y^b)}{Area} - \frac{(M_z^t + M_z^b)}{Area} \\ m_{xz} = 0 \\ m_{yz} = 0 \end{Bmatrix} \tag{A.9}$$

These can be transformed into a symmetric experiment by applying the decoupling **Equations 2.5** on the entire stress vectors corresponding to the $S1$ and $S2$ experiments, resulting in a symmetric and antisymmetric experiment stress vector:

$$\boldsymbol{\sigma^{sym.}} = \begin{Bmatrix} \sigma_{xx} = \frac{1}{2}(R_x^t + R_x^b)/Area \\ \sigma_{yy} = \frac{1}{2}(R_x^t + R_x^b)/Area \\ \sigma_{xy} = \frac{1}{2}\frac{(R_y^t + R_y^b)}{Area} \\ \sigma_{yx} = \frac{1}{2}\frac{(R_y^t + R_y^b)}{Area} \\ m_{xz} = 0 \\ m_{yz} = 0 \end{Bmatrix} \quad \& \quad \boldsymbol{\sigma^{antisym.}} = \begin{Bmatrix} \sigma_{xx} = \frac{1}{2}(R_x^t + R_x^b)/Area \\ \sigma_{yy} = \frac{1}{2}(R_x^t + R_x^b)/Area \\ \sigma_{xy} = \frac{1}{2}\frac{(R_y^t + R_y^b)}{Area} - \frac{(M_z^t + M_z^b)}{Area} \\ \sigma_{yx} = -\frac{1}{2}\frac{(R_y^t + R_y^b)}{Area} + \frac{(M_z^t + M_z^b)}{Area} \\ m_{xz} = 0 \\ m_{yz} = 0 \end{Bmatrix} \tag{A.10}$$

Which can then be decoupled individually to yield the decoupled stress tensors:

$$\boldsymbol{S^{sym.}} = \begin{matrix} S_{xx} = \frac{1}{2}(R_x^t + R_x^b)/Area \\ S_{yy} = \frac{1}{2}(R_x^t + R_x^b)/Area \\ S_{xy} = \frac{1}{2}(R_y^t + R_y^b)/Area \\ T_{xy} = 0 \\ m_{xz} = 0 \\ m_{yz} = 0 \end{matrix} \quad \& \quad \boldsymbol{S^{antisym.}} = \begin{matrix} S_{xx} = \frac{1}{2}(R_x^t + R_x^b)/Area \\ S_{yy} = \frac{1}{2}(R_x^t + R_x^b)/Area \\ S_{xy} = 0 \\ T_{xy} = \frac{1}{2}(R_y^t + R_y^b)/Area - (M_z^t + M_z^b)/Area \\ m_{xz} = 0 \\ m_{yz} = 0 \end{matrix} \tag{A.11}$$

Here, the load is applied aligned with the shear direction of the measured face. Since the shear experiments are combined into a symmetric and antisymmetric experiment, the main load of the symmetric experiment is found in S_{xy}, which changes to T_{xy} for the antisymmetric experiment.

A.3.2. Solving the equilibrium

Looking at **Figure A.1c**, the static equilibrium equations between the sensor and MM sample are found to be:

$$\sum F_{x^+} = F_x - (R_x^t + R_x^b) = 0 \tag{A.12a}$$

$$\sum F_{y^+} = F_y - (R_y^t + R_y^b) = 0 \tag{A.12b}$$

$$\sum M_O = M_z - (M_x^t + M_z^b) - \frac{L}{2}(R_y^t + R_y^b) - \frac{L}{4}(R_x^t - R_x^b) = 0 \tag{A.12c}$$

and that

$$\begin{matrix} F_x = (R_x^t + R_x^b) \\ F_y = -(R_y^t + R_y^b) \\ M_z = (M_x^t + M_z^b) + \frac{L}{2}(R_y^t + R_y^b) + \frac{L}{4}(R_y^t - R_y^b) \end{matrix} \tag{A.13}$$

By substituting the decoupled micropolar stress definitions of **Equation A.11**, these equations can be rewritten to find how the micropolar stresses appear as a function of the measured reaction loads F_x, F_y and M_z. Last, when assuming the two fixed ends of the MM sample (left and right) are loaded equally such that $R_y^l = R_y^r$, these relations become:

$$\boldsymbol{S^{sym.}}: \begin{matrix} S_{xx} = \frac{1}{2}F_x/Area \\ S_{yy} = \frac{1}{2}F_x/Area \\ S_{xy} = -\frac{1}{2}F_y/Area \\ T_{xy} = 0 \end{matrix} \quad \& \quad \boldsymbol{S^{antisym.}}: \begin{matrix} S_{xx} = \frac{1}{2}F_x/Area \\ S_{yy} = \frac{1}{2}F_x/Area \\ S_{xy} = 0 \\ T_{xy} = ((\frac{1}{2} + \frac{L}{2})F_y - M_z)/Area \end{matrix} \tag{A.14}$$

A.4. Rotation equilibrium

For the rotation experiments, shown in **Figure A.1d**, the micropolar stresses on each face are defined to be.

$$S_{xx} = 0 \tag{A.15a}$$

$$S_{yy} = 0 \tag{A.15b}$$

$$S_{xy} = 0 \tag{A.15c}$$

$$T_{xy} = \sum_i M_z^i/Area \tag{A.15d}$$

$$m_{xz} = 0 \tag{A.15e}$$

$$m_{yz} = 0 \tag{A.15f}$$

Here, all faces are fully constrained. Thus, the primary load measurement is T_{xy} for both the clockwise and anticlockwise experiments. Furthermore, it is directly assumed that al faces distribute the reaction loads equally. Thus, the moment contributions of the axial reaction forces on the faces cancel out.

Then, the static equilibrium equations between the sensor and MM sample are found to be:

$$\sum F_{x^+} = F_x = 0 \tag{A.16a}$$

$$\sum F_{y^+} = F_y = 0 \tag{A.16b}$$

$$\sum M_O = M_z - \sum_i M_z^i = 0 \tag{A.16c}$$

By substituting the decoupled micropolar stress definitions of **Equation A.15**, these equations can be rewritten to find how the micropolar stresses appear as a function of the measured reaction loads F_x, F_y and M_z.

$$\begin{matrix} F_x = 0 \\ F_y = 0 \\ M_z = \sum_i M_z^i \end{matrix} \quad \longrightarrow \quad T_{xy} = M_z / Area \tag{A.17}$$

B

Experimental protocol

B.1. Experimental setup

B.1.1. Setting up the rig

1. Fix the rig to the table with M6 Allen bolts.
2. Attach the sensor to the rig, inserting the M3 Allen bolts from below. Make sure the sensor axes are aligned with the square plate.
3. Ensure the bolts keeping the sensor at a given height are slightly loose. The height may need adjusting.
4. Initialize the linear stage now that it can still move freely by booting up LabView with the combined sensor package.
5. Move the linear stage interface suitably in-range to the rig through the LabView interface.

B.1.2. Axial/bending and shear plates

Attaching a sample for the axial, bending or shear experiments.

1. Attach the MM sample to the actuator slots, according to your measurement.
2. Attach the MM sample, with the actuator slots, to the base-plate and ensure the fixed are clamped to a rigid connection.
3. Attach the base-plate, with the MM sample and actuator sliders attached, loosely to the actuator.
4. Attach the base-plate of the experiment, axial/bending or shear, to the sensor, inserting the M3 Allen bolts from above.
5. Ensure the MM is still connected to the actuator. Change the height of the base-plate if it is not properly aligned. Use the steel measurement blocks to make incremental changes and ensure it is all level.
6. Tighten the M3 nut of the actuator interface to the slider.

B.1.3. Rotation plate

Attaching a sample for the rotation experiment.

1. Push M3 contact pins through the pressure-fit internal holes of the MM sample.
2. Attach the MM sample to the base-plate and ensure all outside boundaries are are clamped rigidly to the base-plate.
3. Attach the base-plate of the rotation experiment to the sensor, inserting the M3 Allen bolts from above.
4. Insert the actuator rod through the base-plate, through the sensor, and through the double bearing on the rig-end of the sensor from above.

5. Ensure the ”arms” of the rod are free to rotate and touch the contact pins at the same instant on both the top and bottom of the MM sample.
6. Push the spool attachment onto the actuator rod from the bottom side of the rig. Make sure the large diameter spool faces the ground and that the other side does not quite touch the sensor attachment plate of the rig.
7. Tighten the spool attachment onto the actuator rod using M3 allen bolts.
8. Lead the wire around the spool once or twice and bring the end towards the linear stage actuator interface and attach the wire end to the actuator.
9. Tighten the M3 nut of the actuator interface to the wire end.

B.2. Calibration

Once the samples are set, a calibration has to be performed...

1. Set displacement velocity to 0.1 mm per second (Moderate accuracy setting).
2. Move the linear stage position such that its sensor registers approximately 0 N.
3. Tweak the alignment knobs on the linear stage such that the reaction force sensor measures approximately 0N in the perpendicular axis of actuation (F_x).

B.3. Motion tracking

For the motion tracking, a phone holder is installed on the top of the rig. This holder was printed with the specific dimensions of the authors phone, such that the camera was aligned with the center of the sample in each experiment. All that is there to do is to press record before the experiment is initiated. The motion tracking is then completed in post-processing.

B.4. Experiment protocols

1. Check if the setup is aligned, the actuator and all sensors are operational and the phone camera is in place.
2. Double check that LABView is in relative displacement mode.
3. Press record on the camera.
4. Set the displacement $d = -10$ mm for the axial and bending experiments and $d = -20$ mm for the shear and rotation experiments.
5. Wait for the stage to arrive at the destination, wait at least one second. and then set the displacement to $d = 10$ mm and $d = 20$mm for the axial/bending and shear/rotation experiments respectively.
6. Wait for the stage to arrive at the destination, wait at least one second, set the displacement to $d = 0$mm. Once there wait at least 1 second again.
7. Repeat steps 4-6 at least three more times.
8. After the last repetition, stop the labview programm and stop recording on the video camera.
9. Right click on a grpah and export to excel. Repeat this for all graphs.
10. Copy-paste all data-files into a single excel, each column contains a signal ordered as: $[d, F_{act}, F_x, F_y, F_z, M_x, M_y, M_z]$ and let the rows contain the measured data of each signal.
11. Save this excel according to the experiment name containing at least the geometry, tesselation, and experiment. E.g. create a folder named ”Mr4_2x2”, which describes the geometry and save the excel as ”A1”, describing the experiment.

B.5. Error handling

Whenever the camera did not record, the experimental rig was bumped or a sensor malfunction during an experiment, repeat the experiment.

C

Observations in experiments

Experiment	Node	Observations	Result
A1	Top left	Stuck in actuator. SC with B.L.	$u_x = \phi = 0$, $u_y = d$
	Top right	-	
	Bottom left	Excessive rotation. SC at $d = 9.5$ mm	
	Bottom right	B.C. not clamped	
A2	Top left	Stuck in actuator. SC with B.L.	$u_x = \phi = 0$, $u_y = d$
	Top right	-	
	Bottom left	Excessive rotation. SC at $d = 9.5$ mm	
	Bottom right	B.C. slips at $d = 2.5$ mm	
S1	Top left	B.C. not clamped	
	Top right	-	
	Bottom left	Actuator slip at $d = [-5, -3]$ mm	
	Bottom right	-	
S2	Top left	-	
	Top right	-	
	Bottom left	-	
	Bottom right	-	
B1	Top left	Stuck in actuator.	$u_x = \phi = 0$, $u_y = d$
	Top right	-	
	Bottom left	Excessive rotation.	
	Bottom right	-	
B2	Top left	Stuck in actuator.	$u_x = \phi = 0$, $u_y = d$
	Top right	-	
	Bottom left	Excessive rotation.	
	Bottom right	-	
Rc	Top left	-	
	Top right	-	
	Bottom left	-	
	Bottom right	-	
Rc	Top left	-	
	Top right	-	
	Bottom left	-	
	Bottom right	-	

D

Figures of all results

Table D.1: A table showing the removed offsets

Experiment offsets	F_{act} [N]	F_y [N]	F_x [N]	M_z [Nm]	ϕ^{TL} [rad]	ϕ^{TR} [rad]	ϕ^{BL} [rad]	ϕ^{BR} [rad]
A1	0.15	1.2	3.6	0.047	1.05	1.03	1.05	1.05
A2	0.18	1.4	3.6	0.025	1.07	1.05	1.05	1.06
S1	0.081	0.39	3.7	0.15	−0.49	−0.48	2.64	2.65
S2	0.22	0.45	3.6	0.15	−0.51	−0.49	2.63	2.62
B1	0.10	1.3	3.6	0.043	1.07	1.03	2.63	2.62
B2	0.10	1.4	3.7	0.034	1.06	1.04	2.64	2.62
Rc	−0.024	1.1	3.4	0.060	−0.50	−2.10	1.05	2.65
Rcc	−0.079	1.4	−3.4	0.058	−2.11	−2.07	1.06	2.67

D.1. Sensor data

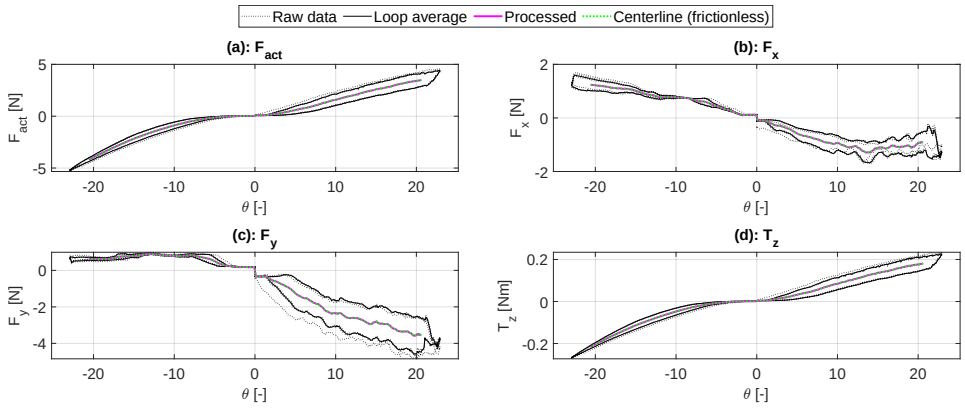

(a) Force-displacement plots of combined experiments Rc and Rcc.

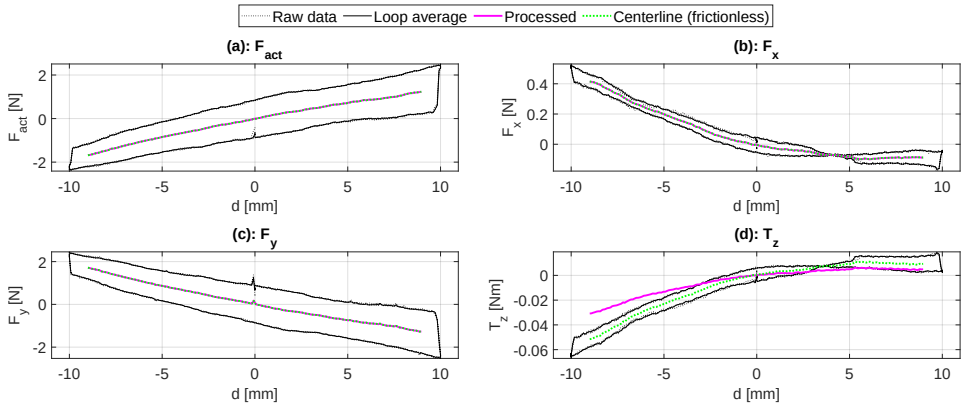

(b) Force-displacement plots of experiment A1.

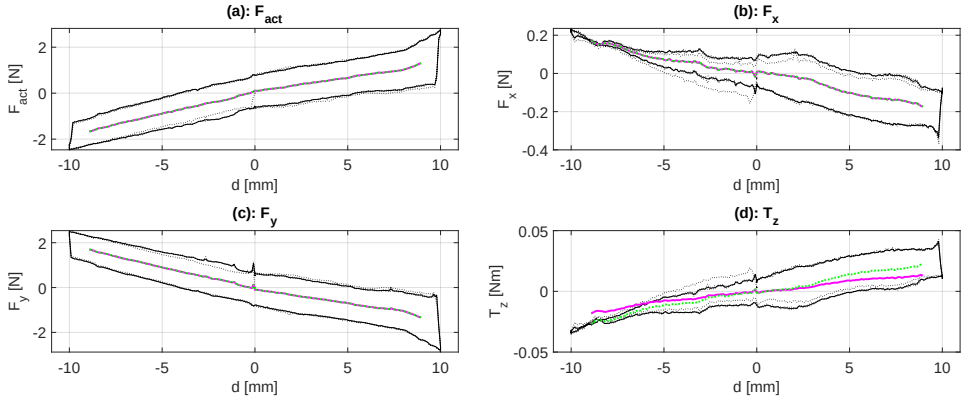

(c) Force-displacement plots of experiment A2.

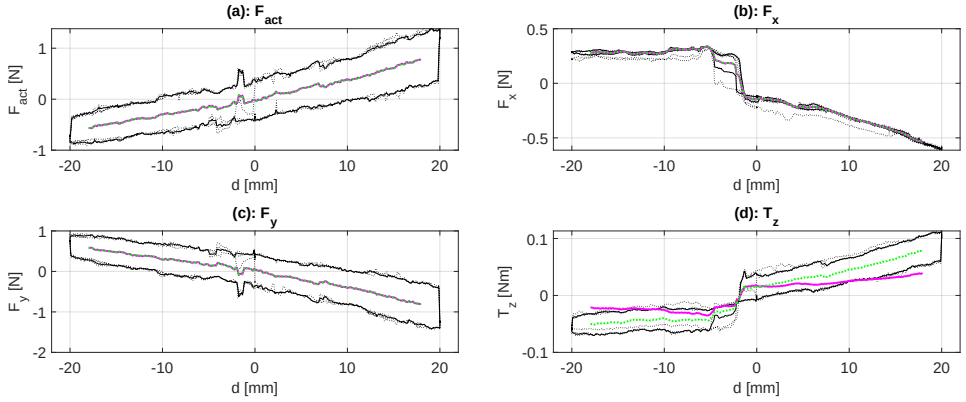

(d) Force-displacement plots of experiment S1.

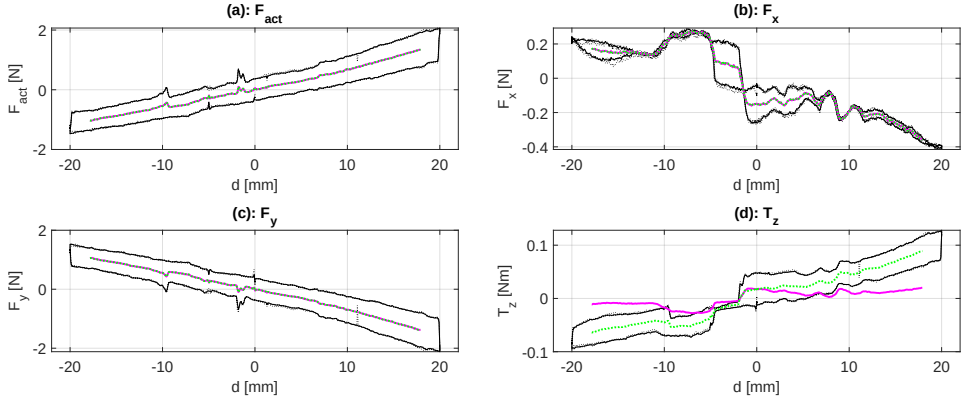

(e) Force-displacement plots of experiment S2.

Figure D.1: Eight simple graphs

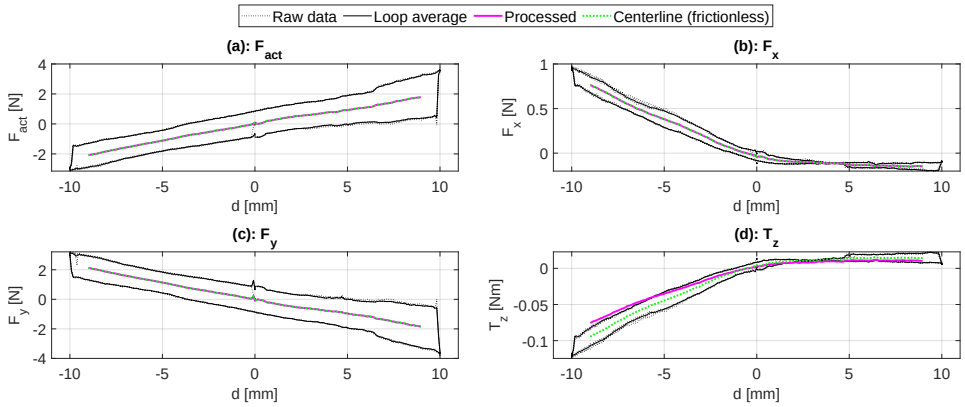

(f) Force-displacement plots of experiment B1.

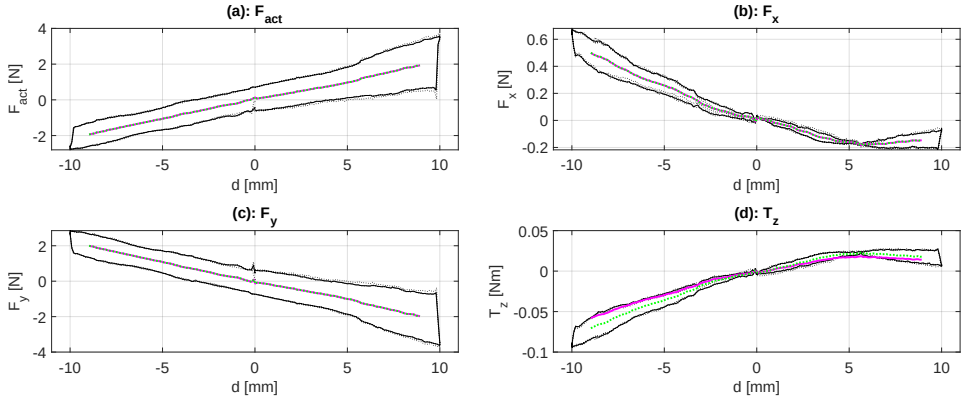

(g) Force-displacement plots of experiment B2.

D.2. Motion tracking data

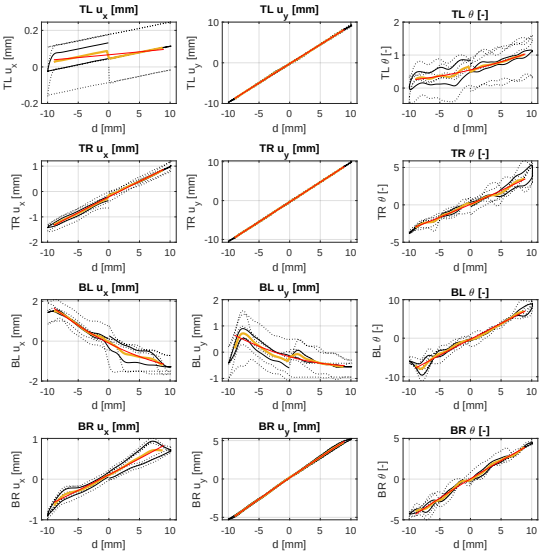

(a) A1 raw analysis

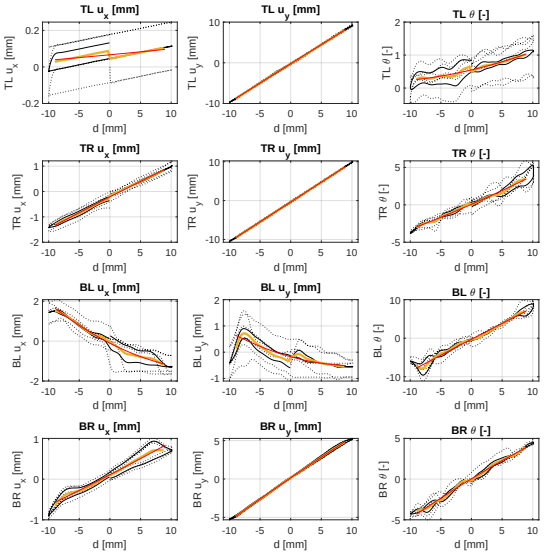

(b) A2 raw analysis

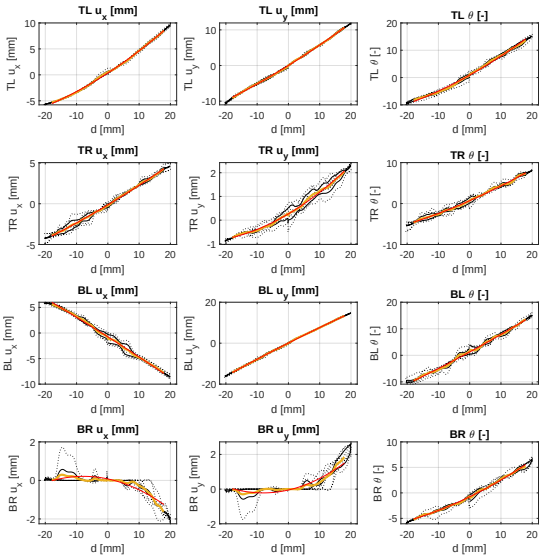

(c) S1 raw analysis

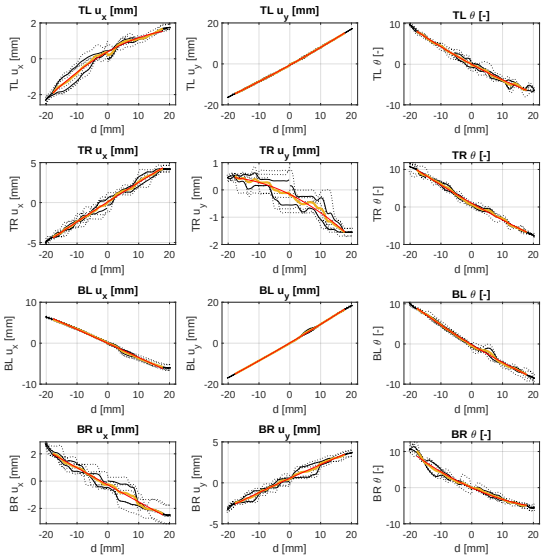

(d) S2 raw analysis

Figure D.2: Eight simple graphs

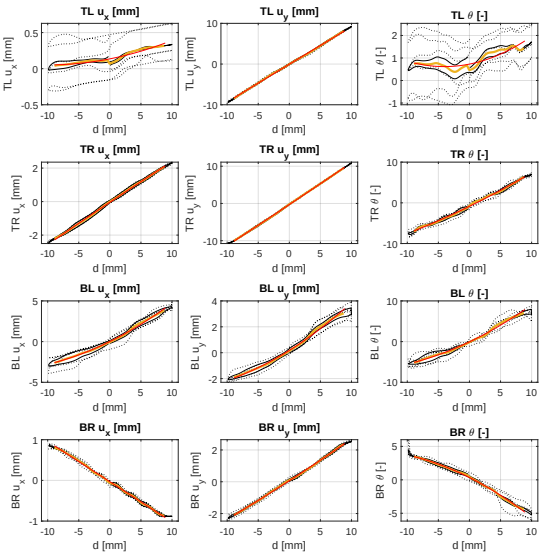

(a) B1 raw analysis

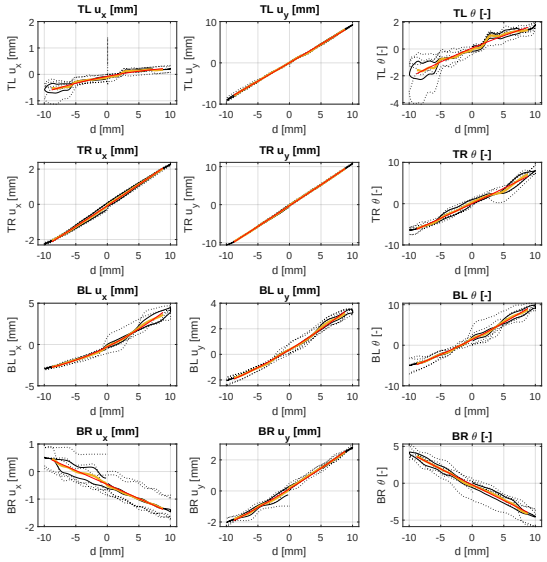

(b) B2 raw analysis

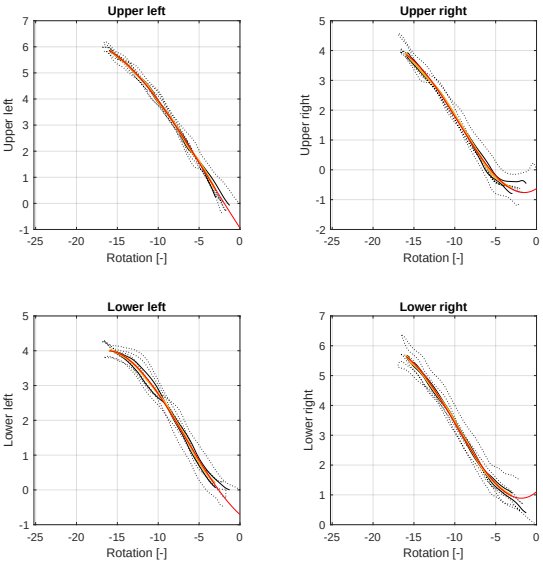

(c) Rc raw analysis

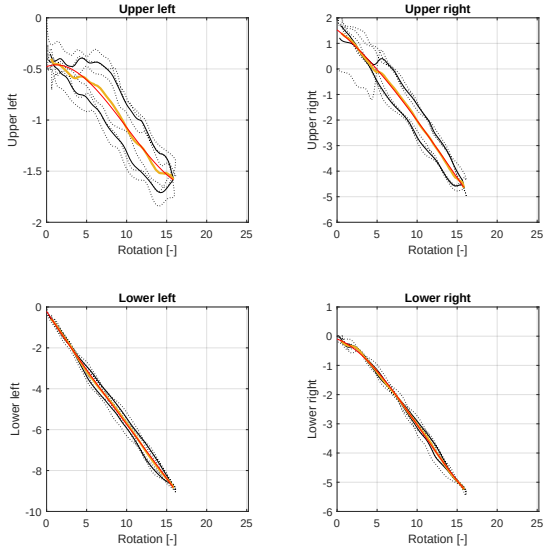

(d) Rcc raw analysis

Figure D.3: Eight simple graphs

E

Solving the system of equations

Now, taking the general form of the decoupled micropolar elasticity tensor presented in **Equation 2.8** and applying the identified strain tensors from **Table 2.4** for each experiment, we can write out the systems of equations for each experiment.

$$\boldsymbol{S^{A1}} = \begin{Bmatrix} S_{xx} \\ \cancel{S_{yy}}^{0} \\ S_{xy} \\ T_{xy} \\ \cancel{m_{xz}}^{0} \\ \cancel{m_{yz}}^{0} \end{Bmatrix} = \begin{bmatrix} c_{11} & c_{14} \\ c_{21} & c_{24} \\ c_{31} & c_{34} \\ c_{41} & c_{44} \\ c_{51} & c_{64} \\ c_{61} & c_{64} \end{bmatrix} \begin{Bmatrix} E_{xx} \\ 2A_{xy} \end{Bmatrix} \quad \& \quad \boldsymbol{S^{A2}} = \begin{Bmatrix} \cancel{S_{xx}}^{0} \\ S_{yy} \\ S_{xy} \\ T_{xy} \\ \cancel{m_{xz}}^{0} \\ \cancel{m_{yz}}^{0} \end{Bmatrix} = \begin{bmatrix} c_{12} & c_{14} \\ c_{22} & c_{24} \\ c_{32} & c_{34} \\ c_{42} & c_{44} \\ c_{52} & c_{64} \\ c_{62} & c_{64} \end{bmatrix} \begin{Bmatrix} E_{yy} \\ 2A_{xy} \end{Bmatrix} \tag{E.1}$$

For symmetric and antisymmetric shear S and A:

$$\boldsymbol{S^{S}} = \begin{Bmatrix} S_{xx} \\ S_{yy} \\ S_{xy} \\ \cancel{T_{xy}}^{0} \\ \cancel{m_{xz}}^{0} \\ \cancel{m_{yz}}^{0} \end{Bmatrix} = \begin{bmatrix} c_{13} \\ c_{23} \\ c_{33} \\ c_{43} \\ c_{63} \\ c_{63} \end{bmatrix} \{2E_{xy}\} \quad \& \quad \boldsymbol{S^{A}} = \begin{Bmatrix} S_{xx} \\ S_{yy} \\ \cancel{S_{xy}}^{0} \\ T_{xy} \\ \cancel{m_{xz}}^{0} \\ \cancel{m_{yz}}^{0} \end{Bmatrix} = \begin{bmatrix} c_{14} \\ c_{24} \\ c_{34} \\ c_{44} \\ c_{64} \\ c_{64} \end{bmatrix} \{2A_{xy}\} \tag{E.2}$$

For B1 and B2:

$$\boldsymbol{S^{B1}} = \begin{Bmatrix} \cancel{S_{xx}}^{0} \\ S_{yy} \\ S_{xy} \\ T_{xy} \\ m_{xz} \\ \cancel{m_{yz}}^{0} \end{Bmatrix} = \begin{bmatrix} c_{12} & c_{14} & c_{15} \\ c_{22} & c_{24} & c_{25} \\ c_{32} & c_{34} & c_{35} \\ c_{42} & c_{44} & c_{45} \\ c_{52} & c_{64} & c_{55} \\ c_{62} & c_{64} & c_{65} \end{bmatrix} \begin{Bmatrix} E_{yy} \\ 2A_{xy} \\ \varphi_{xz} \end{Bmatrix} \quad \& \quad \boldsymbol{S^{B2}} = \begin{Bmatrix} S_{xx} \\ \cancel{S_{yy}}^{0} \\ S_{xy} \\ T_{xy} \\ \cancel{m_{xz}}^{0} \\ m_{yz} \end{Bmatrix} = \begin{bmatrix} c_{11} & c_{14} & c_{16} \\ c_{21} & c_{24} & c_{26} \\ c_{31} & c_{34} & c_{36} \\ c_{41} & c_{44} & c_{46} \\ c_{51} & c_{64} & c_{56} \\ c_{61} & c_{64} & c_{66} \end{bmatrix} \begin{Bmatrix} E_{xx} \\ 2A_{xy} \\ \varphi_{yz} \end{Bmatrix} \tag{E.3}$$

Now, we first solve the elastic constants relating to the symmetric and antisymmetric shear experiments in **Equations E.2**. Applying the stresses definitions in **Appendix A** the elastic constants can be calculated by evaluating at the displacement extremities $d = \pm 10$ mm.

$$\begin{array}{ll} c_{13} = S^S_{xx}/(2E^S_{xy}) & c_{14} = S^A_{xx}/(2A^A_{xy}) \\ c_{23} = S^S_{yy}/(2E^S_{xy}) \quad \& & c_{24} = S^A_{yy}/(2A^A_{xy}) \\ c_{33} = S^S_{xy}/(2E^S_{xy}) & c_{44} = T^A_{xy}/(2A^A_{xy}) \\ c_{43} = c_{53} = c_{63} = 0 & c_{34} = c_{54} = c_{64} = 0 \end{array} \tag{E.4}$$

Then, these elastic constants can be substituted into **Equations E.1**, allowing them to be solved next. First, the set of equations relating to $A1$ becomes:

$$\begin{aligned}
S_{xx}^{A1} &= c_{11}E_{xx}^{A1} + 2c_{14}A_{xy}^{A1} \\
\cancelto{0}{S_{yy}^{A1}} &= c_{21}E_{xx}^{A1} + 2c_{24}A_{xy}^{A1} \\
S_{xy}^{A1} &= c_{31}E_{xx}^{A1} + \cancelto{0}{2c_{34}A_{xy}^{A1}} \\
T_{xy}^{A1} &= c_{41}E_{xx}^{A1} + 2c_{44}A_{xy}^{A1} \\
\cancelto{0}{m_{xz}^{A1}} &= c_{51}E_{xx}^{A1} + \cancelto{0}{2c_{54}A_{xy}^{A1}} \\
\cancelto{0}{m_{yz}^{A1}} &= c_{61}E_{xx}^{A1} + \cancelto{0}{2c_{64}A_{xy}^{A1}}
\end{aligned} \longrightarrow \begin{aligned}
c_{11} &= (S_{xx}^{A1} - 2c_{14}A_{xy}^{A1})/E_{xx}^{A1} \\
c_{21} &= (-2c_{24}A_{xy}^{A1})/E_{xx}^{A1} \\
c_{31} &= (S_{xy}^{A1})/E_{xx}^{A1} \\
c_{41} &= (T_{xy}^{A1} - 2c_{44}A_{xy}^{A1})/E_{xx}^{A1} \\
c_{51} &= c_{61} = 0
\end{aligned} \tag{E.5}$$

And the set of equations relating to $A2$ becomes:

$$\begin{aligned}
\cancelto{0}{S_{xx}^{A2}} &= c_{12}E_{yy}^{A2} + 2c_{14}A_{xy}^{A2} \\
S_{yy}^{A2} &= c_{22}E_{yy}^{A2} + 2c_{24}A_{xy}^{A2} \\
S_{xy}^{A2} &= c_{32}E_{yy}^{A2} + \cancelto{0}{2c_{34}A_{xy}^{A2}} \\
T_{xy}^{A2} &= c_{42}E_{yy}^{A2} + 2c_{44}A_{xy}^{A2} \\
\cancelto{0}{m_{xz}^{A2}} &= c_{52}E_{yy}^{A2} + \cancelto{0}{2c_{54}A_{xy}^{A2}} \\
\cancelto{0}{m_{yz}^{A2}} &= c_{62}E_{yy}^{A2} + \cancelto{0}{2c_{64}A_{xy}^{A2}}
\end{aligned} \longrightarrow \begin{aligned}
c_{12} &= (-2c_{14}A_{xy}^{A2})/E_{yy}^{A2} \\
c_{22} &= (S_{yy}^{A2} - 2c_{24}A_{xy}^{A2})/E_{yy}^{A2} \\
c_{32} &= (S_{xy}^{A2})/E_{yy}^{A2} \\
c_{42} &= (T_{xy}^{A2} - 2c_{44}A_{xy}^{A2})/E_{yy}^{A2} \\
c_{52} &= c_{62} = 0
\end{aligned} \tag{E.6}$$

Lastly, the found elastic constants can be substituted into the equations relating to the bending experiments in **Equations E.3**. Then, the system of equations of $B1$ becomes

$$\begin{aligned}
\cancelto{0}{S_{xx}^{B1}} &= c_{12}E_{yy}^{B1} + 2c_{14}A_{xy}^{B1} + c_{15}\varphi_{xz} \\
S_{yy}^{B1} &= c_{22}E_{yy}^{B1} + 2c_{24}A_{xy}^{B1} + c_{25}\varphi_{xz} \\
S_{xy}^{B1} &= c_{32}E_{yy}^{B1} + \cancelto{0}{2c_{34}A_{xy}^{B1}} + c_{35}\varphi_{xz} \\
T_{xy}^{B1} &= c_{42}E_{yy}^{B1} + 2c_{44}A_{xy}^{B1} + c_{45}\varphi_{xz} \\
m_{xz}^{B1} &= \cancelto{0}{c_{52}E_{yy}^{B1}} + \cancelto{0}{2c_{54}A_{xy}^{B1}} + c_{55}\varphi_{xz} \\
\cancelto{0}{m_{yz}^{B1}} &= \cancelto{0}{c_{62}E_{yy}^{B1}} + \cancelto{0}{2c_{64}A_{xy}^{B1}} + c_{65}\varphi_{xz}
\end{aligned} \longrightarrow \begin{aligned}
c_{15} &= (-c_{12}E_{yy}^{B1} - 2c_{14}A_{xy}^{B1})/\varphi_{xz} \\
c_{25} &= (S_{yy}^{B1} - c_{22}E_{yy}^{B1} - 2c_{24}A_{xy}^{B1})/\varphi_{xz} \\
c_{35} &= (S_{xy}^{B1} - c_{32}E_{yy}^{B1})/\varphi_{xz} \\
c_{45} &= (T_{xy}^{B1} - c_{42}E_{yy}^{B1} - 2c_{44}A_{xy}^{B1})/\varphi_{xz} \\
c_{55} &= m_{xz}^{B1}/\varphi_{xz} \\
c_{65} &= 0
\end{aligned} \tag{E.7}$$

And for the $B2$ experiment

$$\begin{aligned}
S_{xx}^{B2} &= c_{11}E_{xx}^{B2} + 2c_{14}A_{xy}^{B2} + c_{16}\varphi_{yz} \\
\cancelto{0}{S_{yy}^{B2}} &= c_{21}E_{xx}^{B2} + 2c_{24}A_{xy}^{B2} + c_{26}\varphi_{yz} \\
S_{xy}^{B2} &= c_{31}E_{xx}^{B2} + \cancelto{0}{2c_{34}A_{xy}^{B2}} + c_{36}\varphi_{yz} \\
T_{xy}^{B2} &= c_{41}E_{xx}^{B2} + 2c_{44}A_{xy}^{B2} + c_{46}\varphi_{yz} \\
\cancelto{0}{m_{xz}^{B2}} &= \cancelto{0}{c_{51}E_{xx}^{B2}} + \cancelto{0}{2c_{54}A_{xy}^{B2}} + c_{56}\varphi_{yz} \\
m_{yz}^{B2} &= \cancelto{0}{c_{61}E_{xx}^{B2}} + \cancelto{0}{2c_{64}A_{xy}^{B2}} + c_{66}\varphi_{yz}
\end{aligned} \longrightarrow \begin{aligned}
c_{16} &= (S_{xx}^{B2} - c_{11}E_{xx}^{B2} - 2c_{14}A_{xy}^{B2})/\varphi_{yz} \\
c_{26} &= (-c_{21}E_{xx}^{B2} - 2c_{24}A_{xy}^{B2})/\varphi_{yz} \\
c_{36} &= (S_{xy}^{B2} - c_{31}E_{xx}^{B2})/\varphi_{yz} \\
c_{46} &= (T_{xy}^{B2} - c_{41}E_{xx}^{B2} - 2c_{44}A_{xy}^{B2})/\varphi_{yz} \\
c_{56} &= 0 \\
c_{66} &= m_{xy}^{B2}/\varphi_{yz}
\end{aligned} \tag{E.8}$$